An X-ray spectroscopic search for dark matter and unidentified line signatures in the Perseus cluster with Hitomi

Takayuki Tamura[1], **Andrew C. Fabian**[8], **Poshak Gandhi**[2], **Liyi Gu**[3], **Ayuki Kamada** [4], **Tetsu Kitayama**[5], **Michael Loewenstein**[6,11], **Yoshitomo Maeda**[1], **Kyoko Matsushita**[7], **Dan McCammon**[10], **Kazuhisa Mitsuda**[1], **Shinya Nakashima**[3], **Scott Porter**[6], **Ciro Pinto**[8], **Kosuke Sato**[9], **Francesco Tombesi**[6], **and Noriko Y. Yamasaki**[1]

[1] Institute of Space and Astronautical Science, Japan Aerospace Exploration Agency, 3-1-1 Yoshinodai, Chuo-ku, Sagamihara, Kanagawa 229-8510, Japan

[2] Department of Physics & Astronomy, University of Southampton, SO17 1BJ, UK

[3] RIKEN High Energy Astrophysics Laboratory, 2-1 Hirosawa, Wako, Saitama 351-0198, Japan

[4] Center for Theoretical Physics of the Universe, Institute for Basic Science (IBS), Daejeon 34126, Korea

[5] Department of Physics, Toho University, 2-2-1 Miyama, Funabashi, Chiba 274-8510

[6] NASA, Goddard Space Flight Center, 8800 Greenbelt Road, Greenbelt, MD 20771, USA

[7] Department of Physics, Tokyo University of Science, 1-3 Kagurazaka, Shinjuku-ku, Tokyo 162-8601

[8] Institute of Astronomy, Madingley Road, CB3 0HA Cambridge, United Kingdom

[9] Department of Physics, Saitama University, 255 Shimo-Okubo, Sakura-ku, Saitama, 338-8570

[10] Physics Department, University of Wisconsin, Madison, WI 53706, USAS

[11] University of Maryland College Park, Department of Astronomy, 4296 Stadium Dr., College

Park, MD , USA, 20742

*E-mail: tamura.takayuki@jaxa.jp

Abstract

We present results of a search for unidentified line emission and absorption signals in the 2–12 keV energy band of spectra extracted from Perseus Cluster core region observations obtained with the 5 eV energy resolution Hitomi Soft X-ray Spectrometer. No significant unidentified line emission or absorption is found. Line flux upper limits (1σ per resolution element) vary with photon energy and assumed intrinsic width, decreasing from ~ 100 photons cm^{-2} s^{-1} sr^{-1} at 2 keV to < 10 cm^{-2} s^{-1} sr^{-1} over most of the 5–10 keV energy range for a Gaussian line with Doppler broadening of 640 km s^{-1} . Limits for narrower and broader lines have a similar energy dependence and are systematically smaller and larger, respectively. These line flux limits are used to constrain the decay rate of hypothetical dark matter candidates. For the sterile neutrino decay rate, new constraints over the the mass range of 4–24 keV with mass resolution better than any previous X-ray analysis are obtained. Additionally, the accuracy of relevant thermal spectral models and atomic data are evaluated. The Perseus cluster spectra may be described by a composite of multi-temperature thermal and AGN power-law continua. Superposed on these, a few line emission signals possibly originating from unmodeled atomic processes (including Si XIV and Fe XXV) are marginally detected and tabulated. Comparisons with previous X-ray upper limits and future prospects for dark matter searches using high-energy resolution spectroscopy are discussed.

Key words: dark matter — galaxies: clusters: individual (Perseus, A426) — X-rays: galaxies: clusters —

1 Introduction

X-ray spectroscopy has long been used to study the physical state and elemental composition in various astronomical hot plasmas. The advent of high energy resolution instruments in orbit has improved the sensitivity to weak spectral features, and hence the diagnostic power of X-ray spectroscopy. Most recently, the Soft X-ray Spectrometer (SXS; Kelley et al. 2018), the first X-ray calorimeter that collected observations in orbit, onboard the Hitomi observatory

(Takahashi et al. 2018) demonstrated new capabilities by achieving a 5 eV FWHM energy resolution. This represents superior sensitivity and better resolving power above 2 keV than any previous X-ray grating instruments and, by virtue of being non-dispersive, is better-suited for observing extended sources such as clusters of galaxies.

Thanks to these capabilities, Hitomi high-energy resolution spectroscopic analysis may be used to enhance dark matter X-ray searches. There are several reports of putative detections of unidentified X-ray signals, such as Prokhorov & Silk (2010). A recent, much discussed claim is of a line at around 3.5 keV in the Perseus cluster and a stacked sample of clusters by Bulbul et al. (2014). Together with subsequent reports (e.g. Boyarsky et al. 2014; Boyarsky et al. 2015; Neronov et al. 2016 claiming independent detections consistent with the dark matter interpretation, these works have attracted a substantial number of follow-up observational studies with different instruments and objects. Among these are works by Tamura et al. (2015), Sekiya et al. (2016), and others reporting non-detection and disfavoring a substantial part of the claimed 3.5 keV flux range (see Abazajian 2017 for summaries). As discussed in these studies, potential dark matter X-ray signals are expected to be too faint to be resolved by previous X-ray detectors (mostly Charge-Coupled Devices; CCDs). In fact, the claimed 3.5 keV signals have line equivalent widths of about 1 eV, corresponding to a $< 1\%$ excesses above continuum, generally smaller than the instrumental calibration uncertainties (typically 10%). Even the deepest and targeted searches such as Ruchayskiy et al. (2016) and Cappelluti et al. (2018) may have marginally detected a signal at 3.5 keV but failed to disentangle various possibilities due to limited CCD energy resolution.

The unidentified X-ray line signals may originate from dark matter radiative decay, as originally proposed by Abazajian et al. (2001), with the keV sterile neutrino being one long-standing candidate (see Adhikari et al. 2017 for a review). The 3.5 keV claims stimulate theoretical consideration of sterile neutrino production mechanisms, as well as many other dark matter candidate particles, conceived in order to explain unidentified X-ray signals. These in turn indicate how parameter space can be constrained or new physics searches expanded exclusively by X-ray spectroscopy of cosmic dark matter systems. Many, but by no means all, these dark matter candidates tend to behave as warm dark matter, suppressing sub-galactic structure formation by free-streaming. Probes of small-scale matter clustering such as a number count of satellite galaxies (e.g. Cherry & Horiuchi 2017) and Lyman-α forest measurements (e.g., Baur et al. 2017 and references therein) play a complementary role in searching for proposed dark matter candidates (e.g., Bae et al. 2018 for further discussion).

In addition to enhancing the quality of X-ray searches for dark matter, improvements

3

of spectroscopic sensitivity provide an opportunity to measure faint signals from relatively rare elements and previously unresolved atomic features (Hitomi Collaboration et al. 2017). For example, Bulbul et al. (2014) discussed possible 3.5 keV line origins in atomic features from K, Ar, or Cl ions; while, Gu et al. (2015) proposed an origin from charge exchange emission. Disentangling such mixtures of processes from these dominant thermal emission is only accessible via high resolution spectroscopy, as discussed thoroughly in Kaastra et al. (2008) and Smith et al. (2014).

There are now a few calorimeter data sets of relevance to searches for dark matter and other weak features. Figueroa-Feliciano et al. (2015) used sounding rocket calorimeter spectra with energy resolution of 11–23 eV, covering a wide sky area, with a short exposure time of 106 s towards an anti-center Galactic plane region. They revealed no 3.5 keV signal. Aharonian et al. (2017) used the SXS Perseus spectra to search for the 3.5 keV signal, deriving an upper limit inconsistent with previous claimed detections in Perseus. Utilizing the latest versions of ATOMDB and SPEX plasma codes, Hitomi Collaboration (2018c) (hereafter H2018-T) found that the same Perseus spectra may be described by simple thermal models with an average temperature of 4 keV without any significant residuals in the 2–15 keV energy band. Furthermore, Hitomi Collaboration (2018d) (hereafter H2018-A) evaluated spectral fit residuals and the accuracy of the model input atomic physics. Hitomi Collaboration (2018a) examined the SXS spectra of the Crab Nebula, a spectrally featureless calibration source, searching for previously undetected line emission or absorption signatures. We use this result to estimate the calibration uncertainty bf of the instrumental effective area.

The highest quality spectrum with the Hitomi SXS is of the core of Perseus, a nearby relaxed galaxy cluster and the X-ray brightest extra-galactic extended source (Hitomi Collaboration 2016). Making use of the extensive plasma modeling conducted in Hitomi papers cited above, we further examine the spectra for weak line emission and absorption signals at the energies of both known and unknown features. We present the first line search results over a broad X-ray energy band (2–12 keV) from a massive dark matter structure at energy resolution better than any previous X-ray analysis. We resolve a number of strong and weak atomic line emission features but find no significant unidentified line emission nor absorption. We derive upper limits used to constrain the sterile neutrino decay rate and compare our results with previous X-ray limits. Discussion is made on the limitations of a weak line search with an instrument with high energy resolution but modest collecting area.

Throughout this paper, we assume the following cosmological parameters: $H_0 = 70$ km s^{-1}Mpc^{-1}, $\Omega_m = 0.3$, and $\Omega_\Lambda = 0.7$. One arc-minute corresponds to 21.1 kpc at the Perseus

cluster redshift, z = 0.017284 (Hitomi Collaboration 2018b). Unless otherwise stated, we use the 68% (1σ) confidence level for errors and single-line signal detection significance levels without accounting for the number of independent energy trial bins (i.e., the look elsewhere effect) , and express X-ray energies in the observed (redshifted) frame.

2 Observations and data analysis

2.1 Observations and spectral extraction

Th Perseus cluster was observed four times with the Hitomi SXS in 2016 February and March. These observations are used in the series of papers described in section 1. Detailed descriptions of the Hitomi observatory and the SXS instrument are are found in Takahashi et al. (2018) and Kelley et al. (2018), respectively. Hitomi's X-ray telescope references include Okajima et al. (2016) and Maeda et al. (2018).

In H2018-T we processed and extracted the relevant spectral and responses files which are used herein. We describe the method briefly below. To process data and response files, we use the HEAsoft version 6.21, Hitomi software version 6, and calibration database version 7 (Angelini et al. 2018).

We use Observations 2 (obsid 100040020), 3 (100040030, 100040040, 100040050), and 4 (100040060) with a total exposure time of 289 ks. These observations cover the cluster central core and are denoted as the 'Entire' core in H2018-T and shown in their figure 1. There was another observation (Obs 1) offset by about $3'$ and with an exposure time of 49 ks. Its total flux is fainter by a factor of about 3 and its spectral shape differs in comparison to the other observations. Therefore we do not use this offset data for this study. Combined with the X-ray focusing mirror, the SXS has a $3' \times 3'$ field of view with an angular resolution of $1'.2$ (half power diameter) and covers the energy range of 2–12 keV. We applied event screening based on the pulse rise time versus energy tuned for the wider energy coverage and selected only the high primary grade events, in which the best spectroscopic performance is achieved. We applied pixel-by-pixel redshift correction and gain correction using a parabolic function, as shown in appendix 1 of H2018-T.

2.2 Basic spectral analysis methods

The redistribution matrix file (RMF) and auxiliary response file (ARF) for spectral analysis are generated by `sxsmkrmf` and `aharfgen`, respectively. We use two ARFs for extended cluster emission and point source AGN components. In H2018-T we examined three separate ARFs

with different effective area calibration corrections, finding the Crab ARF (tuned with the Crab spectra as defined in H2018-T)

as the best description of the data for the `AtomDB` spectral model. Accordingly, we use this ARF in the following analysis.

Energy bin sizes for spectral and response (RMF and ARF) files are all 1 eV. No further binning is applied for the spectral fitting, except for plotting purposes. Spectral fits are performed using the Xspec package (version 12.9.1h; Arnaud 1996) with the modified C-statistic (Cash 1979). To model the cluster plasma emission, we use the atomic database `AtomDB` version 3.0.9 (Smith & Brickhouse 2001).

2.3 Backgrounds

Non X-ray background (NXB; Kilbourne et al. 2018) spectra are produced from the night earth observations using `sxsnxbgen` and used in the spectral fitting. Table 1 lists identified and expected features in the NXB spectra.

The cosmic X-ray background is estimated to have an intensity of 3×10^{-4} and 3×10^{-5} in counts s^{-1} keV^{-1} over the SXS field of view at energies of 2 and 10 keV, respectively. These are well below 1% and 0.15% of the source counts at these energies. We therefore ignore this background in the following analysis. The source and estimated NXB spectra are shown in figure 2 of H2018-T.

2.4 Analysis method - A blind line search

We search the SXS spectrum for emission and absorption features above the plasma model over a broad range of possible line position following previous methods used with high energy resolution spectroscopy (e.g., Rasmussen et al. 2007). This is sometimes referred to as a sliding box or blind search. This method was also employed for the Perseus X-ray spectra in Tamura et al. (2015) and Aharonian et al. (2017).

2.4.1 Initial test with a Line-free CIE model

As an initial test to check for prominent line features, we use a single temperature CIE (Collisional Ionization Equilibrium) model without any atomic line emission.[2] Spectral residuals are fitted with Gaussian line components with a fixed intrinsic line width at 2 eV. We detect several strong (e.g., Fe He-line triplet) and weak (e.g., He-like Cr) features. All signals with

---

[2] For this model we use SPEX with option "ion ignore".

Table 1. Expected instrumental features in the SXS background spectra.

Line [*]	Energy (eV)	note
Al Ka	1486	
Mn Ka	5895	Strongest.
Mn Kb	6490	
Ni Ka	7470	
Cu Ka	8048	
Au La	9671	
Au Lb	11510	
Ag Ka	22163	Not clear in the NXB.

Edge [♯]	Energy (eV)	note
Al K	1559.6	
Si K	1839	
Au M	[†]	Mirror, M1-5
Te (52) L	4939 (L1)	Weak
Au (79) L	11919(L3)	Mirror
Hg (80) M	2295(M5), 2385(M4), 2847 (M3)	Escape edge energies

[*] The line features are taken from Kilbourne et al. 2018.

[♯] The edge energies are taken from the LBNL X-Ray Data Booklet[1]. [†] Au edge positions are as follows, 2206(M5), 2291(M4), 2743(M3), 3148(M2), 3425(M1), 14353(L1), 13734(L2), 11919(L3) in eV.

statistical significance larger than 3σ can be identified with atomic transitions expected from a 2–6 keV CIE plasma, as already shown in published Hitomi papers. No significant unidentified line emission is found. In the Appendix, we show a spectral plot with annotated identifications (figure 15).

2.4.2 Baseline model - local-wide-band fits

We determine baseline spectral models with physically reasonable parameters to describe the data accurately in the following wide and narrow bands fits. Based on detailed spectral fitting in H2018-T we found the spectrum to be reproduced by two temperature CIE for the cluster component and a power-law for the AGN emission, along with AGN parameters obtained by Hitomi Collaboration (2018e). These components are modified by a Galactic absorption column density of 1.38×10^{21} cm^{-2}.

Instead of a multi-temperature model suitable for a wide energy band, we use single-temperature models ('tapec' in XSPEC) with changing parameters tuned for each local energy band. We fit the spectrum separately for energy ranges delimited at 1.8, 2.7, 3.7, 6.4, 8.7, and

15.0 keV. The energy band from 6.25–6.32 keV , which includes Fe-I emission from the AGN, is ignored in all cases.

The parameters determined at this step are temperatures (for continuum and for atomic lines), metal abundances, cluster redshift, velocity dispersion, and CIE normalization. Other parameters are held fixed. In the 7.7–7.8 keV energy band that includes both Fe and Ni strong line emission we allow Fe and Ni abundances to vary independently. In other cases, a single metal abundance (represented by Fe) is let free assuming solar abundance ratios.

2.4.3 Gaussian Line flux - narrow band fits -

We add a Gaussian line component ('zgauss' in XSPEC) on top of the wide-band model and determine the best-fit line flux allowing both positive (emission) and negative (absorption) values.

Along with the line position E_{Line}, the intrinsic line width (Gaussian sigma; σ_{Line}) is an important but unknown parameter. We first test the fitted parameters and method with a fixed $\sigma_{\mathrm{Line}} = 3$ eV (subsection 2.4.4 and 3.1.2). Following this, we search for line signals from plasma or dark matter with energy-dependent σ_{Line} varying as $V_{\mathrm{dis}}/c \times E_{\mathrm{Line}}$, where V_{dis} is a Doppler velocity dispersion of the emitter or absorber varying from 0 km s^{-1} to 1600 km s^{-1} with a step of 160 km s^{-1} , and c is the speed of light. Figure 1 shows this relation.

At a plasma temperature of ~ 4 keV, atomic thermal broadening is 80 and 120 km s^{-1} for Fe and S ion lines, respectively. For plasma lines, where will be an additional turbulent velocity component of about 200 km s^{-1} , as measured by Hitomi Collaboration (2018b). The line of sight velocity dispersion of the cluster galaxies is about 1300 km s^{-1} (Kent & Sargent 1983). The assumed V_{dis} brackets these velocity ranges.

Among the source (cluster and AGN) parameters, only the cluster CIE component normalization is left free. Line signals are searched over a fixed energy grid of 5 eV spacing. For each E_{Line} , a limited energy range ($E_{\mathrm{Line}} \pm \Delta E_{\mathrm{narrow}}$) is used.

We use $\Delta E_{\mathrm{narrow}}$ as wide as $10 \times (\sigma_{\mathrm{ins}}^2 + \sigma_{\mathrm{Line}}^2)^{1/2}$, where σ_{ins} is the constant instrumental energy resolution of 2.1 eV.

For each E_{Line} , we determine (1) a best-fit flux (the Gaussian component normalization), and (2) detection significance (S) as defined as

$$S = \sqrt{\Delta C} = \sqrt{C_1 - C_0}, \tag{1}$$

where C_1 and C_0 are C-statistic values for no line and best-flux line models, respectively. These values are assumed to have a χ^2 distribution.
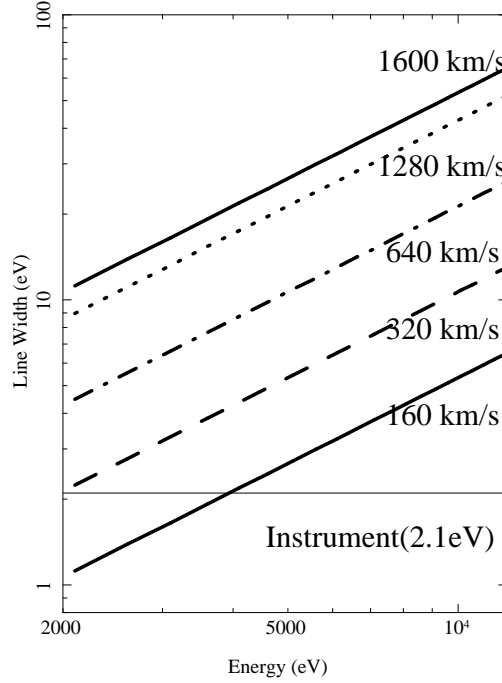
Fig. 1. The relation between the line energy (E_{Line}) and intrinsic line width (σ_{Line}) for different velocity dispersion values (V_{dis}), i.e., $\sigma_{\mathrm{Line}} = V_{\mathrm{dis}}/c \times E_{\mathrm{Line}}$. The horizontal line indicates the instrumental resolution at 2.1 eV.

2.4.4 Fitting energy ranges and energy bin grids

We checked the effect of different energy ranges ($\Delta E_{\mathrm{narrow}}$) for the narrow band fit on the line flux limit. Changing $\Delta E_{\mathrm{narrow}}$ from the default ± 50 eV (for $\sigma_{\mathrm{Line}} = 3$ eV) to ± 25 eV or ± 100 eV had no significant effect on the resulting distribution of S or line flux limits.

We also checked the effect of adopting a finer energy grid. As an example, figure 2 shows a result with an energy grid of 1 eV. We find no significant variation over 5 eV energy bins, confirming that the 5 eV energy bin size is small enough to detect a line feature with $\sigma_{\mathrm{Line}} > 3$ eV.

This limit is satisfied over most of the energy parameter space and $\sigma_{\mathrm{Line}} > 320 \mathrm{km\ s}^{-1}$ (see figure 1; > 3 keV). Therefore energy grids finer than 5 eV are expected to provide line search results consistent with the 5 eV ones.
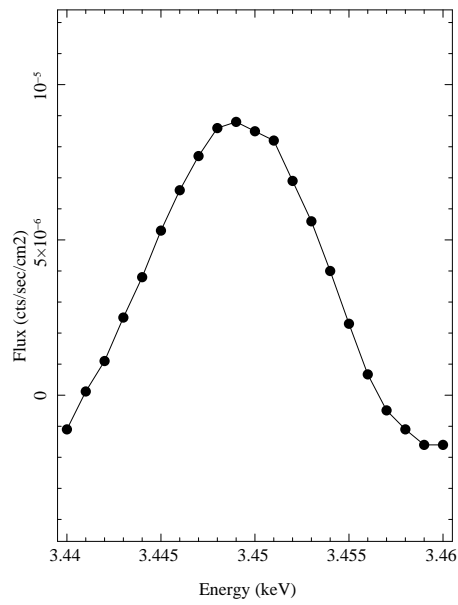
Fig. 2. Best-fit line flux with a finer energy grid of 1 eV at a limited energy range and σ_{Line} = 3 eV. For our main results, we use an energy grid of 5 eV spacing. The plotted energy range represents a typical positive fluctuation. The peak flux corresponds to detection significance $S = 3.1$, which is statistically insignificant considering a large number of trial energy bins (see subsection 3.3.2 regarding statistical evaluation). This plot indicates that the effective width of line detection is wider than 2-3 eV and that no new signal will be found by using an energy grid sharper than 5 eV. See text for further explanation.

3 Results

3.1 Line flux limits

The wide-band fitting results and associated plasma emission models are shown in figures 7-12. The same data and similar fitting results are given in H2018-T and H2018-A.

3.1.1 Residuals around atomic lines

The best-fit line temperatures for the 1.8–2.7–3.7–6.4–8.7–15.0 keV bands are 3.4, 3.6, 3.6, 3.9, and 3.9 keV, respectively.

This increasing temperature trend toward higher energy bands reproduces the multi-temperature emission observed in H2018-T and other studies. H2018-T found some differences in line strengths between the best-fit single and two temperature CIE models, particularly in He-like S and Ar, and Fe Lyα transitions. These differences are up to 10–20% in flux. We find no significant residuals at these positions (e.g., figures 8). Consequently, even if we instead use two CIE models for the local bands, we expect no significant improvement in goodness of fit, and hence no change in the line search results.

3.1.2 Flux limit profiles

A line search result with $\sigma_{\mathrm{Line}} = 3\,\mathrm{eV}$ is shown in figure 3. The best-fit line fluxes (f_{best}) fluctuate statistically over a small range of energy bins between positive and negative values. To estimate the 1σ upper limit profile of line *emission* fluxes we use positive 1σ statistical uncertainties (Δf_+). Compared with these values, standard upper limits ($f_{\mathrm{limit}} = f_{\mathrm{best}} + \Delta f_+$; including both emission and absorption) are larger or smaller by the f_{best} value which statistically fluctuate between positive and negative values. Figure 4 shows f_{best} and the resulting upper limit profile of line emission. This estimate is close to the standard *positive* upper limit averaged over energy ranges.

There are a number of line-like excesses in the upper limit flux profiles (figure 4). These are associated with strong plasma atomic lines in the source emission. Strong source line emission increases background counts for additional faint line detection and decreases sensitivity for the line search.

Figure 5 compares the results when fixing V_{dis} at specific values.

Panel (b) shows upper limits in unit of line equivalent width (EW) computed relative to the source flux (cluster and AGN emission). Absorption like features, e.g., at around 6.7 keV, are due to the source line emission. These line flux limits (f) can be converted into a decay rate (Γ) for an arbitrary dark matter particle of mass m_{DM} by

$$f \simeq 9.3 \text{ photons cm}^{-2}\text{s}^{-1}\text{sr}^{-1} \frac{1}{(1+z)^3} \left(\frac{\Sigma_{\text{DM}}}{10^3 M_\odot \text{pc}^{-2}} \right) \left(\frac{\Gamma}{10^{-27} \text{ s}^{-1}} \right) \left(\frac{m_{\text{DM}}}{\text{keV}} \right)^{-1}, \quad (2)$$

where z and Σ_{DM} are the source redshift and dark matter surface density. To compute Γ from f we adopt $\Sigma_{\text{DM}} = 1750 \ M_\odot \ \text{pc}^{-2}$ for the Perseus core (Aharonian et al. 2017) and assume that emitted photons have an energy $m_{\text{DM}}c^2/2$ as expected for sterile neutrino dark matter.
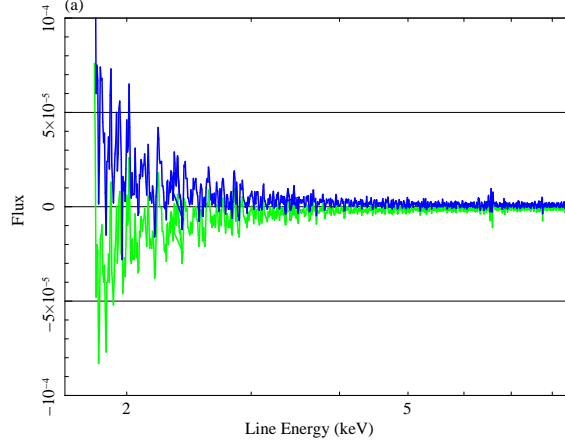
Fig. 3. The line search result with $\sigma_{\text{Line}} = 3$ eV. Statistical 1σ upper and lower limits are shown as different colored lines. The y-axis units are in counts s^{-1} cm^{-2}.
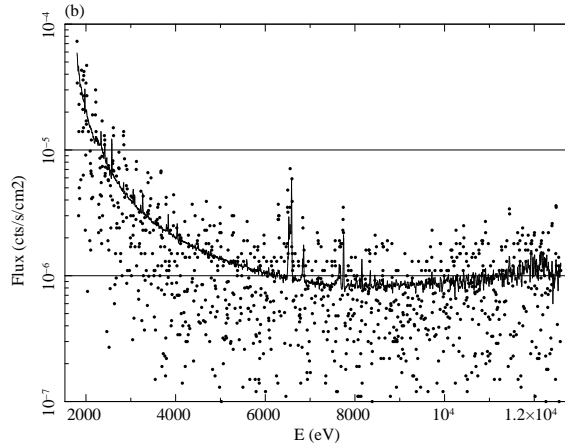

Fig. 4. The best-fit flux (same data with figure 3; f_{best}) and positive 1σ statistical error (Δf_+) are shown by dot marks and the line, respectively. The latter is used as an estimate of the 1σ upper limit flux of line emission.

3.1.3 Different line widths

We examine flux limit profiles among models with different values of σ_{Line} (figure 5). Flux limits for the broader lines are larger than those of the narrow ones in most energy ranges. These
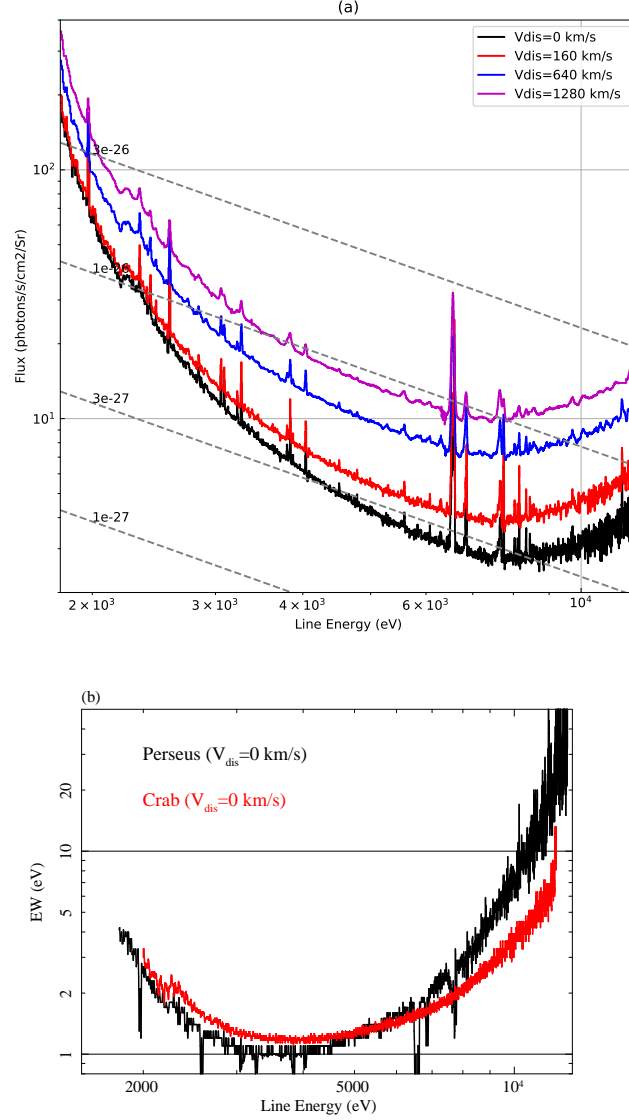
Fig. 5. (a) The estimated 3σ upper limit flux in units of photons s^{-1} cm $^{-2}$ sr $^{-1}$ (Line Unit; LU). Results with different σ_{Line} values are shown. Limits with a number of different velocity dispersion values are marked by different colored lines for a given sets of line energies. Dashed lines indicate corresponding dark matter decay rate in units of s^{-1} given by equation 2. (b) The line flux limits are converted into line EW relative to the source flux (cluster and AGN emission). Results from the Crab observations (Hitomi Collaboration 2018a) are also shown.

relative differences can be approximately explained by a difference in effective energy resolution combining instrumental and source widths. When the line detection sensitivity is limited by background fluctuations, its limit flux is approximately proportional to the square root of the energy resolution. In the actual limits based on spectral fitting, the size of the fitting energy range, $\Delta E_{\mathrm{narrow}}$, also affects the uncertainty of the continuum flux and hence the line flux sensitivity.

13

Table 2. SXS observations of the Perseus core

and Crab*.

Energy (keV)	2	4	10
Perseus (cts/s/keV)	0.05	0.4	0.02
(cts/eV/297 ks)	15	120	4
Crab (cts/s/keV)	3	20	1
(cts/eV/9.7 ks)	30	200	10

* Counts of continuum emission and exposure

times are given.

3.2 The Crab Nebula spectrum and systematic uncertainty

To evaluate systematic errors from the effective area calibration, we use the SXS Crab Nebula observations. Using those observations, Hitomi Collaboration (2018a) performed a spectral line search similar to ours. They used intrinsic line widths (σ_{Line}) fixed at a range of velocities from $\sigma_{\mathrm{Line}} = 0$ to 1280 km s^{-1} . As shown in table 2, the Crab photon counts are about twice those in Perseus over the energy band. The spectrum is intrinsically featureless and hence cleaner than that of Perseus over most of the energy band. These make the Crab data the best and only observations for this purpose. Figure 6 shows comparisons of residuals in terms of best-fit line EW from the Perseus and Crab spectra.

The line flux amplitude limits in the Crab spectrum are smaller than or comparable to those in Perseus over all energy ranges. This is expected due to the better photon statistics in the Crab. This allows us to use the Crab residuals to estimate the systematic error associated with calibrations of the effective area and other instrumental features.

In the Crab spectra, as presented in detail by Hitomi Collaboration (2018a), there are no residuals stronger than the typical statistical noise level ($< 1 - 2$ eV in line EW). We also find no clear positive or negative features common to both spectra. These indicate that any uncalibrated instrumental features are too small to affect the line search significantly within the statistical limit of the Crab observations.

From this comparison, we identify some line features *brighter* than the Crab residuals intrinsic in the Perseus spectrum. One clear example is at around 6300 eV, which is the Fe-I K line from the AGN. These can have astronomical origins and are examined in the next subsection.

We check possible systematic errors associated with time variable response calibrations by using only the Perseus Obs 3 with an exposure time of about a half (146 ks) of the combined one (Obs 2,3, and 4). With representative σ_{Line} values of 160, 640, and 1280 km s^{-1} , we find

no new detection (detection significance $S > 3.5$) nor significant change of S over all energy bins. In other words, time variable calibration uncertainties are too small to change the result from the combined observations.

3.3 Line feature identification

3.3.1 Identified residuals

As shown in the detection significance profiles (figures 7-12), there are ranges of energy bins showing large detection significance (e.g., $S > 3$) of emission or absorption. Here we identify two systematic residuals clearly associated with strong atomic line features.

(1) Around Fe I K at 6280-6300 eV: These originate from the AGN as studied by Hitomi Collaboration (2018e). These are caused by inaccurate modelling of the Fe I K line in the narrow band fitting.

(2) Around the strongest Fe Heα complex at 6450-6620 eV: Those at lower energies (around 6500 eV) may be due to inaccurate plasma thermal and/or atomic modeling as examined in Hitomi Collaboration (2018d). Those on the upper tail of the Fe Heα resonance (around 6620 eV) may be due to inaccurate modelling of plasma (Doppler) velocity structure as discussed in Hitomi Collaboration (2018b). Around this and other strong line features possible calibration errors of the detector response can additionally contribute to observed residuals.

These systematic effects make the detection of weaker features highly model-dependent around strong atomic line features.

When the broader line widths (> 640 km s^{-1}) are assumed, these contaminations affect results around the wider energy bands. We do not use the energy ranges given above for the line search.

3.3.2 Possible line emission features

Apart from the known systematic residuals stated above, there are energy bins showing large detection significance value ($S > 3.2$) as listed in Table 3. To identify line emission signals from the cluster plasma, lower significance ($S > 2.5$) emission signals with $\sigma_{\mathrm{Line}} = 160$ km s^{-1} or 320 km s^{-1} are additionally given. Note that strong line velocities from the cluster plasma were measured at 100–200 km s^{-1} using the same SXS data (e.g. Hitomi Collaboration 2018b). In the appendix (figures 16-19), zoom-in views of spectra around some of these marginal signals are shown. Among them, there are two false signals at 1970 eV (Si) and 7755 eV (Fe), which are on modeled plasma transitions and hence caused by uncertainties on those model emissivities.

The maximum values of S associated with emission and absorption signals are 3.5 and

3.6, respectively. To evaluate these statistical significance considering the look elsewhere effect (e.g., Sekiya et al. 2016), we assume a trial factor computed as the numbers of energy bins [$\sim (1.7–11.5)$ keV divided by 5 eV] times velocity bins (10), which is about 2×10^4. By multiplying the Gaussian probability values by this factor, we predict the number of false positive chances with $S > 3.5$ to be 10 for each emission and absorption signal over the searched energy and velocity space. With this large trial factor, a significant detection corresponding to $> 99\%$ confidence (false positive of 0.01) requires $S > 5$. Therefore any detected signals in the full energy bands including those in Table 3 (not already associated with known systematics in subsection 3.3.1) are consistent with statistical fluctuations. We also confirm that the S distributions obtained are approximately consistent with those from statistical variations. Based on these we conclude that we find no significant detection of any new line emission or absorption feature.

We searched for signals by fixing E_{Line} and σ_{Line} in grids of 5 eV and 160 km s^{-1} , respectively. Based on spectral fitting residuals and S profiles as functions of E_{Line} and σ_{Line} (figures 7-12), no new and significant signal (e.g., $S > 5$) is expected even when taking E_{Line} and σ_{Line} as free parameters. We do not attempt to search for signals with $\sigma_{\text{Line}} > 1600$ km s^{-1} [$> (20 - 100)$ eV], where the SXS is less sensitive than previous CCD observations with much larger grasp.

The signals listed above are not statistically significant detections but hints of possible features. We provide possible identifications with atomic or instrumental features, guided by atomic line lists in H2018-A and the `SPEX` package (version 3.03; Kaastra et al. 1996). In the Appendix (table 6) we give a list of transitions associated with these identifications.

We note possible detections of atomic line emission from high-n to the ground shell emission in Si XIV, Fe XXV, and Ni XXVIII (table 3). These can be caused by charge exchange in the Perseus core. Fe XXV associated with charge exchange in the same data set was previously reported in H2018-A, where another hint of detection from S XVI at ~ 3.4 keV (1.6σ) was shown along with a spectral analysis and discussion of the emission mechanism.

3.3.3 Line absorption features

Excluding the energy ranges of the strong plasma lines, mentioned in subsection 3.3.1 and Si Lyα at 1970 eV, there are several absorption features with $S > 3.2$ listed in table 3.

Some of these are associated with strong plasma or background lines. As mentioned above, these are not statistically significant and too faint to examine further in regards to their possible origin.

The best-fit line fluxes fluctuate symmetrically between positive (emission) and nega-tive (absorption) values (figure 3). Therefore, upper limits on absorption strength (in flux or equivalent width) would have a profile similar to those of the emission features shown in figure 5.

3.3.4 Cross-identifications with previous X-ray line searches

For cross-identifications with our new potential line lists (table 3), we check previous line search results. No cross-identified signal is found.

Using deep Suzaku observations , Tamura et al. (2015) searched for line features from the Perseus cluster. Within the 2–6 keV energy band, they found $> 3\sigma$ signals at 3350, 4100, and 5810 eV. In our list there is no signal close to these energies. Prokhorov & Silk (2010) reported a possible unidentified line at 8.7 keV in Suzaku Galactic center spectra. Koyama et al. (2014) reported fainter line-like feature at 9.4 keV and 10.1 keV in Suzaku Galactic bulge spectra. Sekiya et al. (2016) analyzed a large collection of Suzaku blank-sky observations (excluding the Galactic center) in the 0.5–7 keV energy band and found line-like features with 2–3σ statistical significance at 600, 900, 1275, 4925, and 5475 eV. No coincident signal close to these energies is found in our search.

Table 3. Possible line signal measurements and identifications.

(1) Energy	(2) Energy	(3) Velocity	(4) Flux	(5) EW	(6) S	(7) comments
eV	eV (rest)	km s^{-1}		eV	σ	
			$> 3.2\sigma$ emission			
2610	2655	1120-1280	3.7	3.4	3.2	Si XIV high-n (CX, Nr=60), Figure 16
2840	2889	480	2.0	2.1	3.4	excess of S He β [Ap], Figure 16
7550	7680	960–1440	0.8	9.7	3.3	Figure 16
10215	10392	0	0.2	15.3	3.5	Close to the next one
10910	11099	0	0.3	16.6	3.3	Figure 16
			$> 3.2\sigma$ absorption			
1970	2004	160	-10.0	-2.1	-3.4	uncertainties with Si Lyα emission
7755	7889	0	-0.4	-2.3	-3.6	uncertainties with Fe line, Figure 17
8710	8861	0	-0.2	-3.8	-3.5	Figure 16
8840	8993	0	-0.2	-3.9	-3.4	
10230	10407	160	-0.4	-10.5	-3.3	near background feature (Figure 12), Figure 19
10655	10839	0	-0.2	-6.7	-3.2	Figure 16
			$> 2.5\sigma$ and $\sigma_{\mathrm{Line}} = 160, 320$ km s^{-1} emission			
2840	2889	320	1.3	1.4	2.6	see above
3675	3739	320	0.8	1.5	2.9	Figure 18
5260	5351	320	0.4	1.9	2.5	Figure 18
7555	7686	320	0.3	3.9	2.6	see above
7735	7869	160	0.4	2.5	3.0	Figure 17
8620	8769	320	0.4	6.8	2.7	Figure 18, Fe XXV (CX)
10255	10432	160	0.3	11.6	2.6	see above, Figure 17
10425	10605	160	0.3	13.9	2.8	Ni XXVIII (CX, Nr=36),Zn XXIX (Nr=10), Figure 17

(2) Rest-frame energy with the cluster redshift.

(3) Line width in velocity. (4) Line equivalent width.

(5) In units of 10^{-5} counts cm^{-2} s^{-1}. A minus value in flux and detection significance indicates an absorption signal. (6) Detection significance. This is single-line signal detection significance level without correction for the look-elsewhere effect.

(7) In some cases, possible identification with atomic transitions are given. See the Appendix (Table 6) for a list of possible identification transitions. 'Nr' in parentheses is the SPEX line number given in Table 6. See also spectral plot for expected emissivities for some signals. Ap: Energies and other parameters are given in H2018-A. CX denotes charge exchange emission.
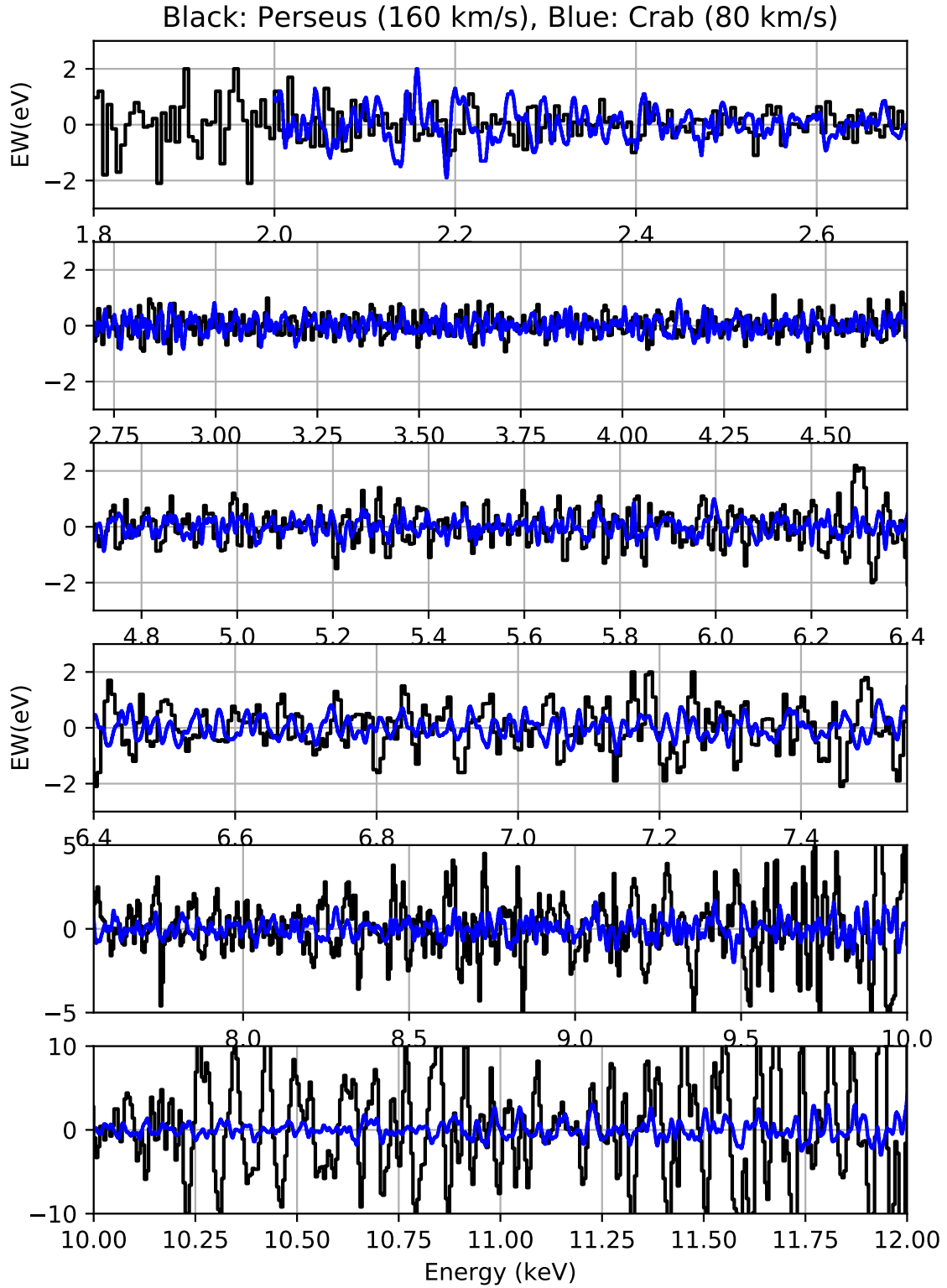
Fig. 6. Line search results in terms of the best-fit line intensity in EW (eV). The Perseus and Crab results are shown in black and blue colors. For the Perseus and Crab fitting, respectively, $\sigma_{\mathrm{Line}} = 160 \ \mathrm{km \ s}^{-1}$ and $80 \ \mathrm{km \ s}^{-1}$.
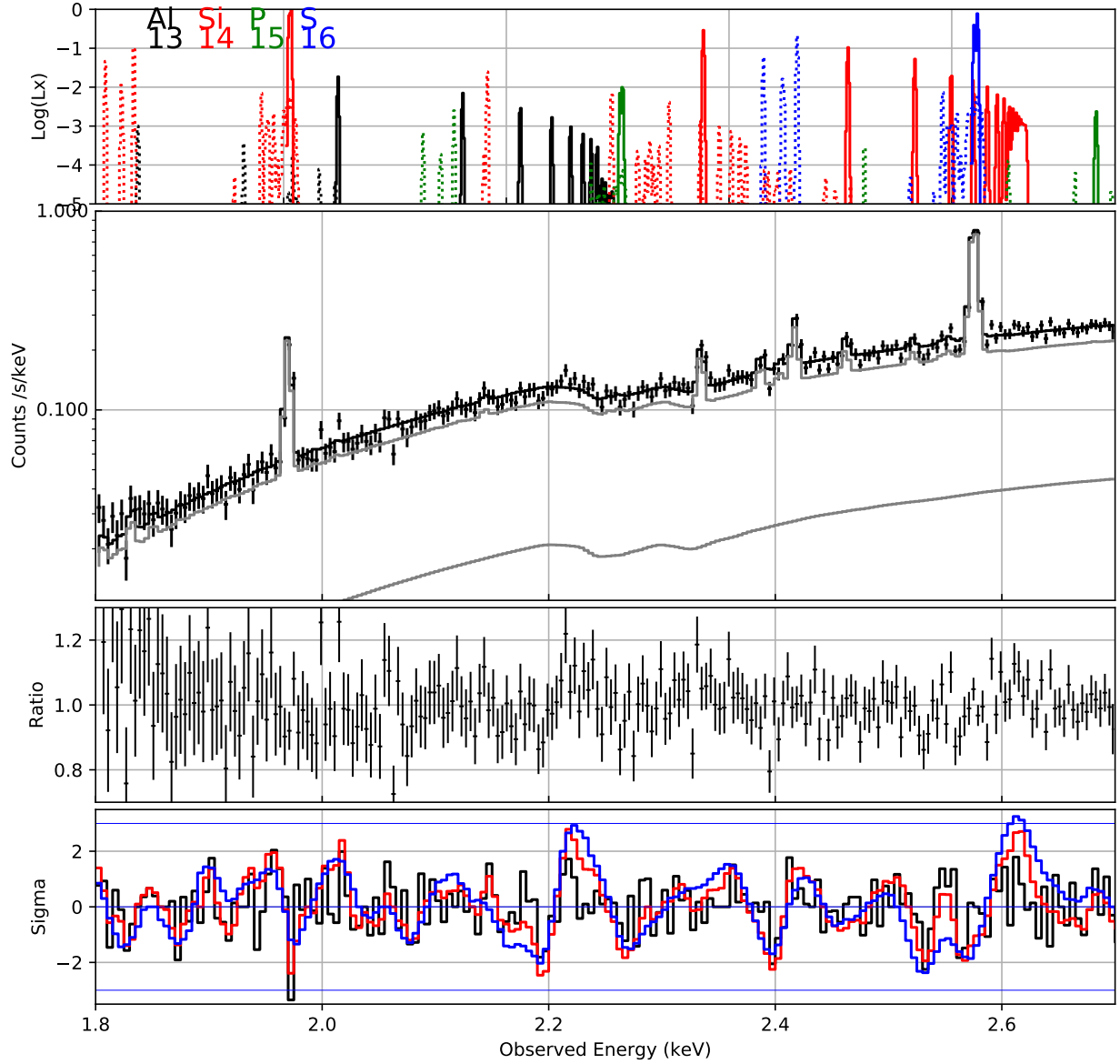
Fig. 7. (Top) Line emission emissivity model in log scale from a limited number of element ions are shown by different colors as denoted by element names and numbers. Different ionization emission are shown by different line styles, e.g., H-like (solid), He-like (dotted). We used the SPEX model with temperature of 4 keV, the solar metal abudance ratio. The x-axis (rest-frame energy) is shifted to match other panel ones (observed energy). The line model in this panel is similar to but not identical to the model used for the other panels. The energy bin size is 1 eV. (Second panel) The observed spectrum along with the best-fit local model (one-temperature APEC). For this and ratio plot, the energy bin sizes are 1–4 eV. (Third panel) The data to model (shown in the second panal) ratio. (Bottom panel) Line detection significance for each energy bin in terms of $(S = \Delta C)^{1/2}$ (in unit of σ). Positive and negative values are for emission and absorption. Results with σ_{Line} = 160, 640, and 1280 in $\mathrm{km\ s^{-1}}$ are shown by black, red, and blue colors, respectively. The X axis is the energy grid of 5 eV spacing.
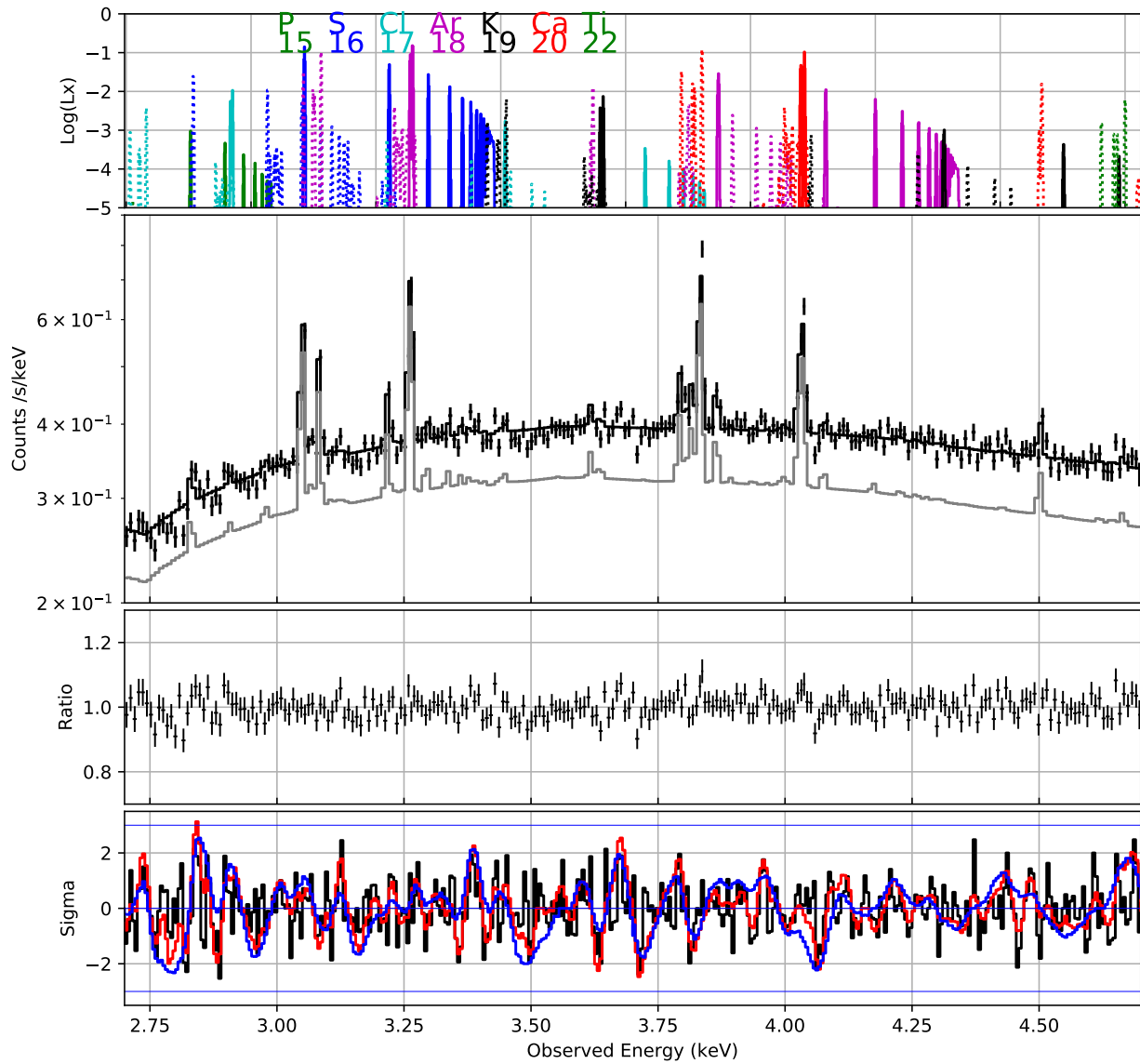
20

Fig. 8. Same plots as previous one, but for the energy range of 2.7–4.7 keV. The energy bin sizes for data and ratio plots are 1–8 eV.
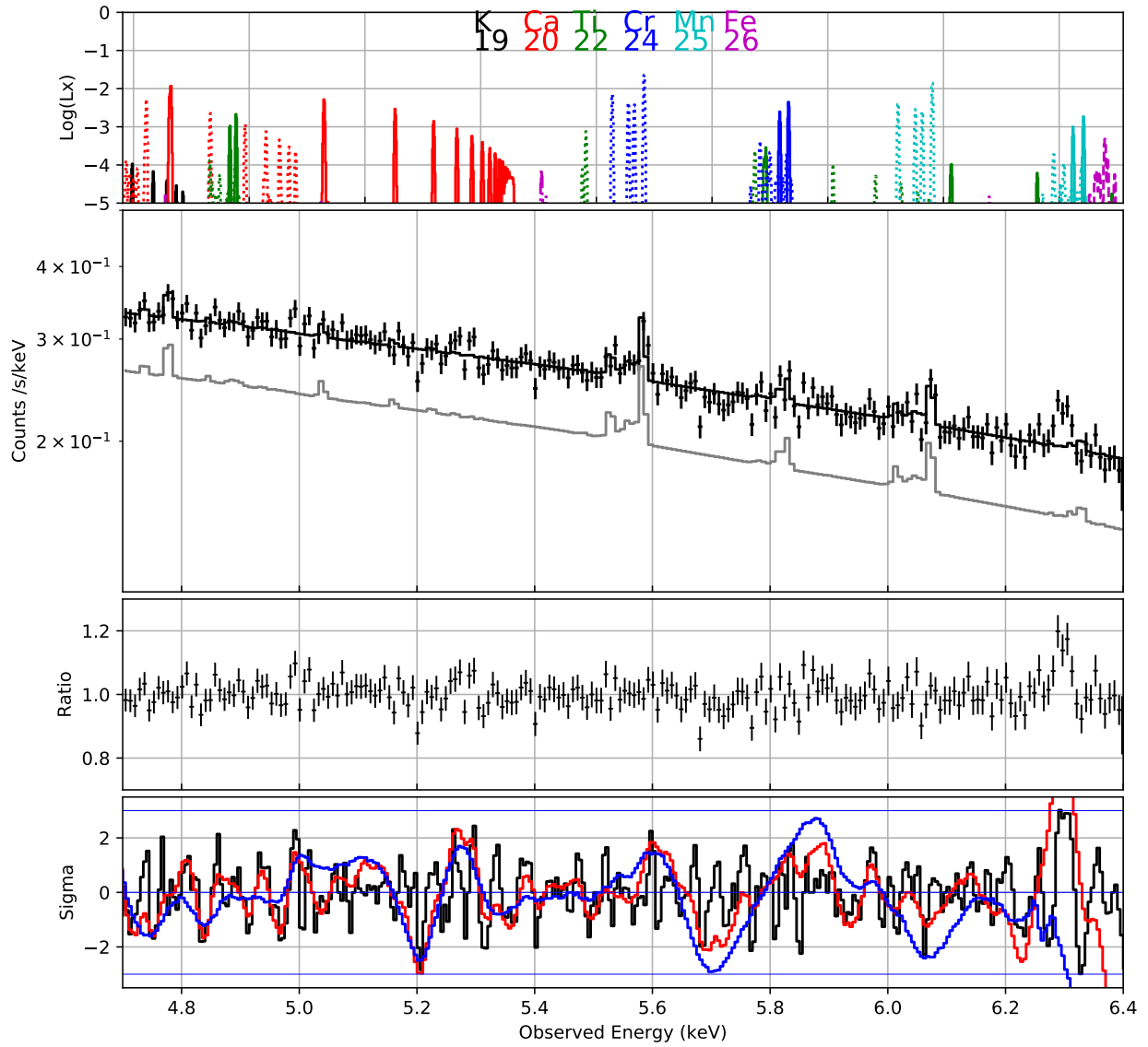
Fig. 9. Same plots as previous one, but for the energy range of 4.7–6.4 keV. The significant excess around 6.3 keV is originated from Fe I K emission of the Perseus AGN.
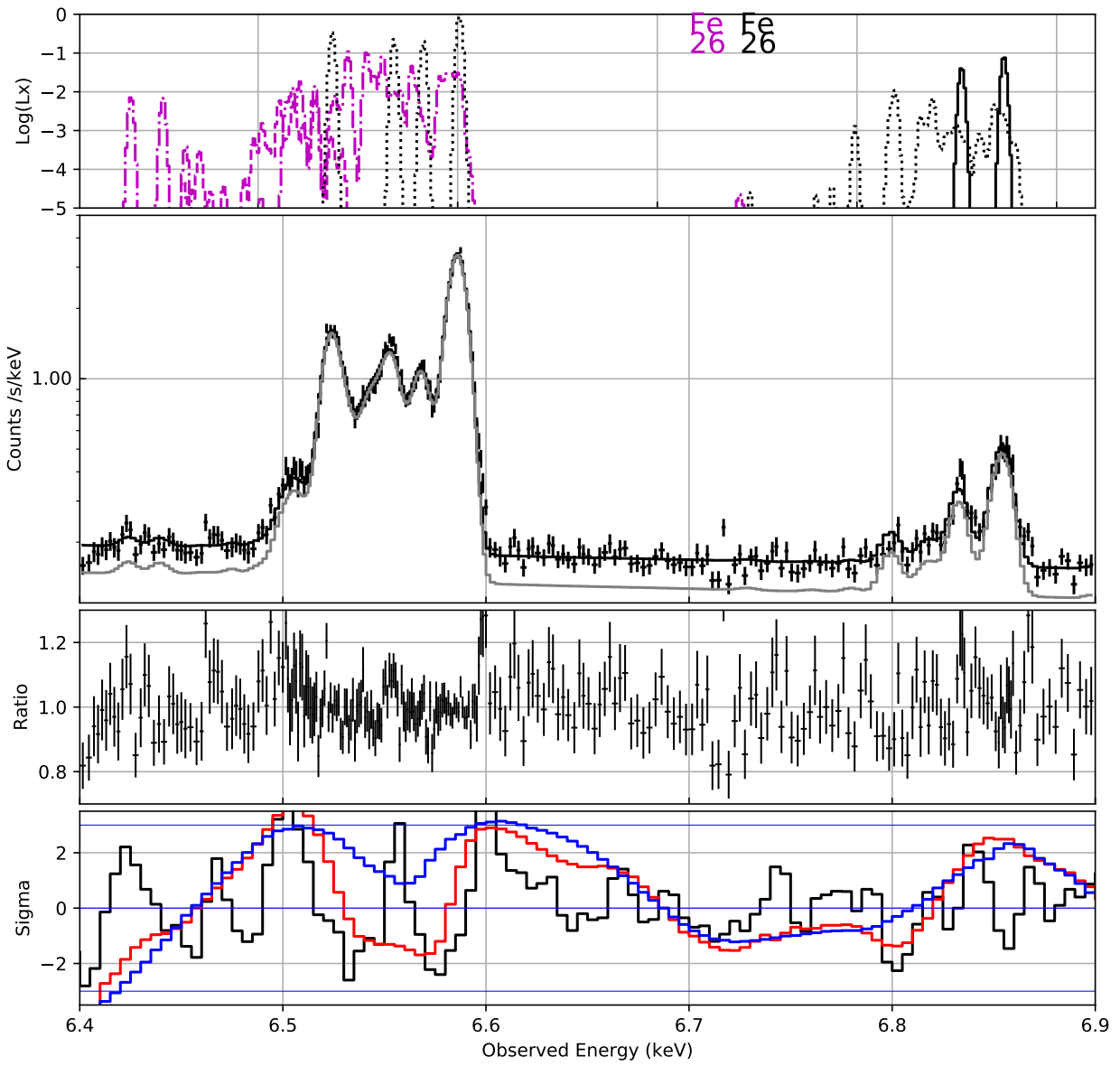
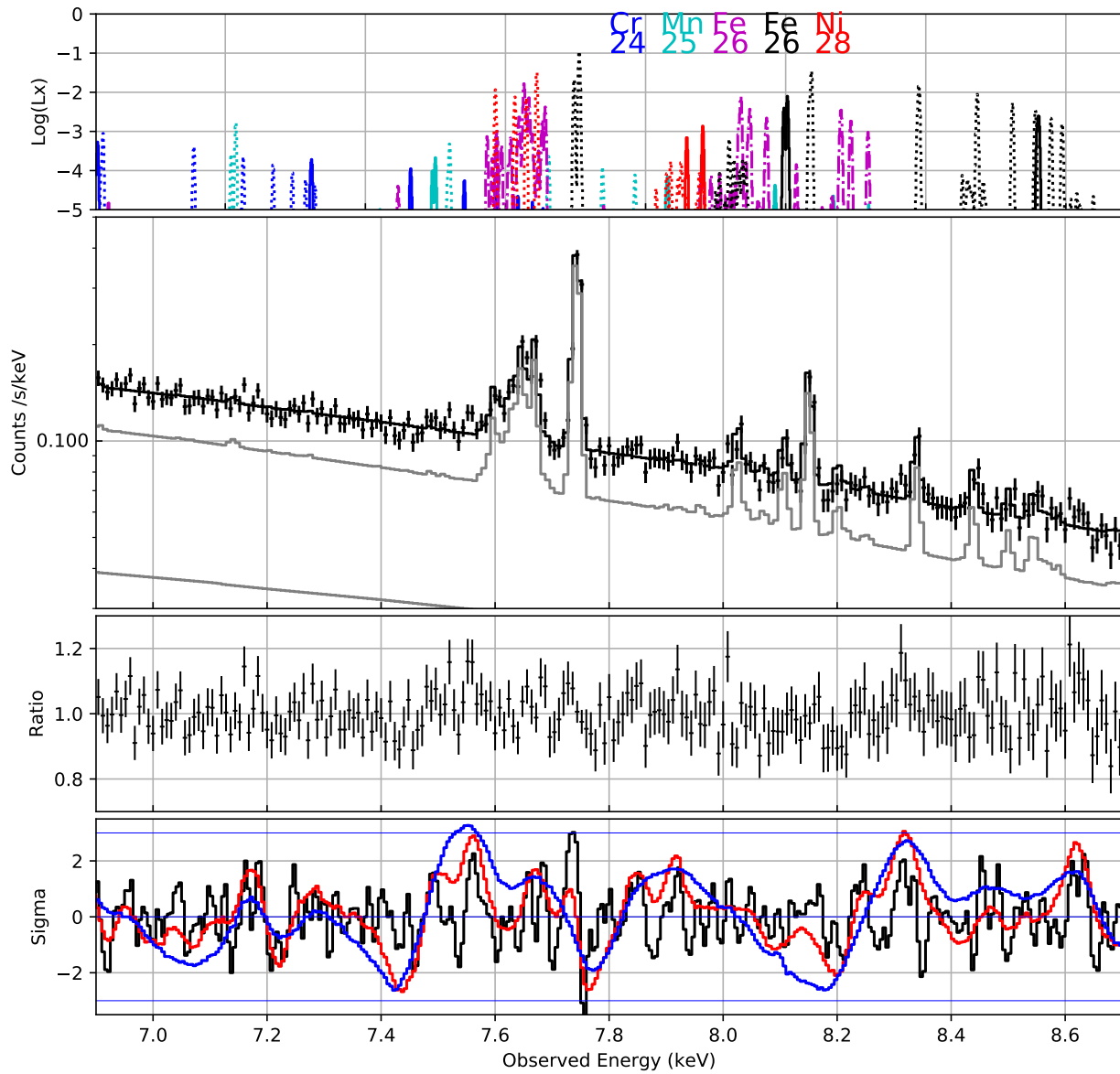**Fig. 10.** Same plots as previous one, but for the energy range of 6.4–6.9 keV.

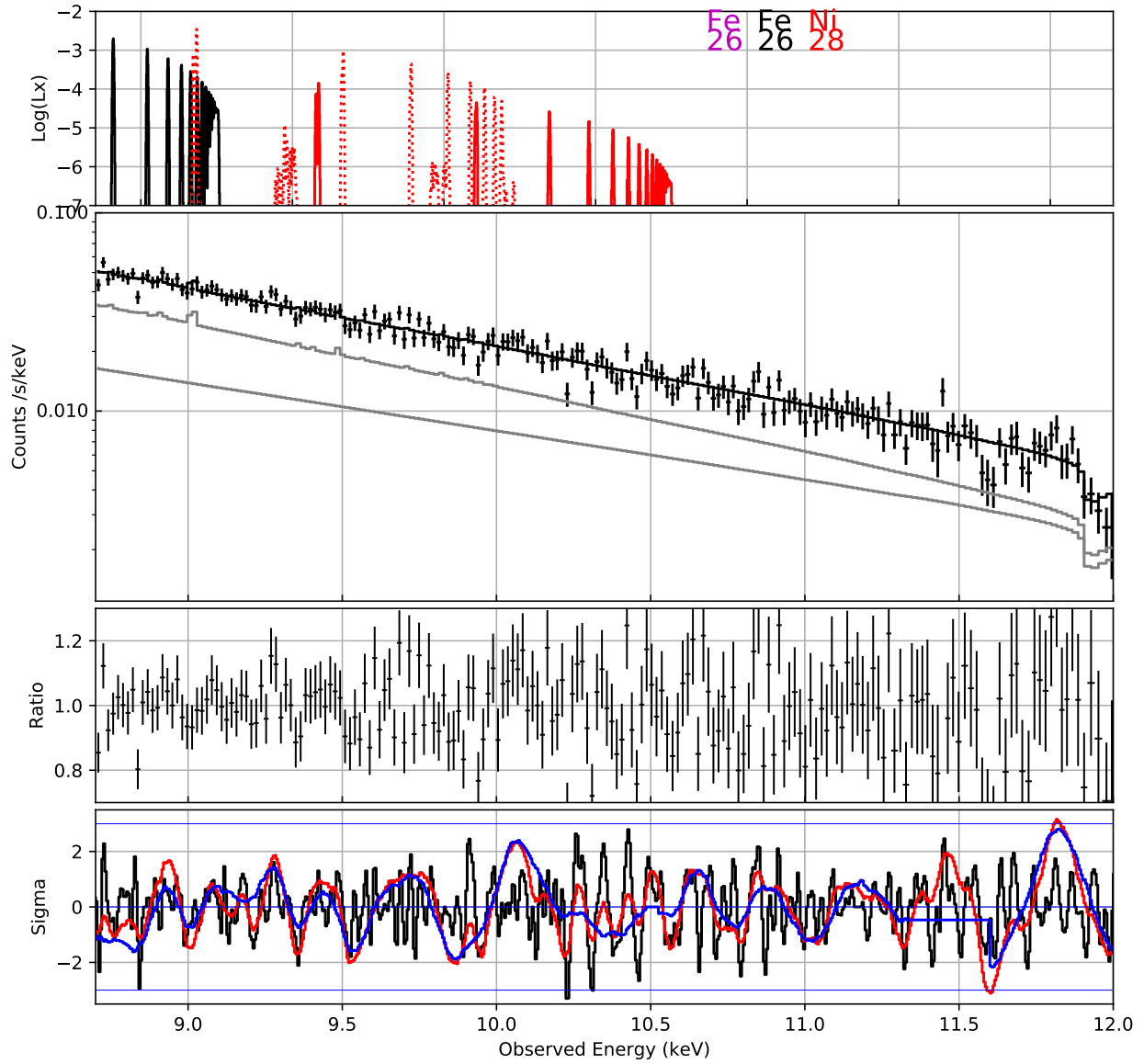**Fig. 11.** Same plots as previous one, but for the energy range of 6.9–8.7 keV.

Fig. 12. Same plots as previous one, but for the energy range of 8.7–12.0 keV and the energy bin sizes for data and ratio plots of 1–16 eV.

4 Discussion

4.1 Comparisons with previous searches

Here, we compare our line search results with previous studies.

4.1.1 Absolute flux estimation

To calculate absolute line flux and density values (figure 5), we assume (1) that all the observed photons originate from the $3' \times 3'$ sky region corresponding to the SXS extraction area, and (2) that the effective area may be approximated by the ARF simulated for a point source at the detector center. The centrally-peaked surface brightness distribution of the cluster and the angular resolution of $1'.2$ (half power diameter) result in the photon spatial distribution after the telescope mixing to have an extension not significantly wider than that of point source. The telescope vignetting reduction within the small field of view is less than 5–10% (Iizuka et al. 2018). In addition, the point source approximation for the ARF results in a flux to be $\sim 10\%$ below that using the Chandra image by Aharonian et al. (2017). Considering these points, we estimate our absolute flux uncertainty to be less than 20–30%, neglecting any additional error terms due to uncertainties e.g., in the pointing accuracy and stability and approximate treatment of the gate valve transmission (Kelley et al. 2018).

4.1.2 Hitomi previous report around 3.5 keV (Aharonian et al. 2017)

Using the same data set and similar analysis method, Aharonian et al. (2017) conducted a line search around 3.5 keV. We compare the published result (their figure 3) with ours at the same energy, and find consistency in the upper limit profile. Aharonian et al. (2017) identified an "excess at 3.44 keV (rest-frame)" at the position of a high-n transition of S XVI and the "dip" at 3.5 keV. We confirm these features (figure 8), but again at low significance.

4.1.3 The SXS Crab search

In figure 5 we compare limits on the line flux equivalent width (EW) from the Crab (Hitomi Collaboration 2018a) [3] We calculate 1σ uncertainties by taking the propagated error on the mean. with the current Perseus result by considering profiles of statistical error in EW (ΔEW). For the background limited case where number of line photon counts (C_{line}) are much less than the "background" (i.e.,cluster continuum) counts (C_{bgd}), i.e., $C_{\mathrm{line}} \ll C_{\mathrm{bgd}}$,

$$\Delta\mathrm{EW} \sim \Delta C_{\mathrm{Line}}/C_{\mathrm{cont}} \propto \sqrt{2C_{\mathrm{bgd}}}/C_{\mathrm{bgd}} \propto C_{\mathrm{bgd}}^{-1/2}. \tag{3}$$

On the other hand, in the photon limited case where $C_{\mathrm{line}} \gg C_{\mathrm{bgd}}$,

---

[3] For this plot, line flux errors and continuum flux provided by M.Tsujimoto are use to calculate the EW limit.

$$\Delta\mathrm{EW} \sim \Delta C_{\mathrm{Line}}/C_{\mathrm{cont}} \propto \sqrt{C_{\mathrm{line}}}/C_{\mathrm{bgd}} \propto C_{\mathrm{bgd}}^{-1}. \tag{4}$$

The adopted spectral fitting method may also affect the limits.

Below 6 keV, limits from the two observations are comparable. Above this energy, the Perseus observations results in larger $\Delta\mathrm{EW}$ than Crab.

At higher energy, the Perseus limit increases more rapidly than the Crab limit. This is probably caused by the photon limited factor, C_{bgd}^{-1}, since for these energies the Perseus counts are down to less than 10 counts per resolution element.

4.1.4 The Suzaku Perseus limit

We compare our SXS Perseus cluster results with those from the Suzaku XIS (CCD) in Tamura et al. (2015) (hereafter T2015). Table 4 compares the respective observational parameters. Figure 13 shows line flux limits from the two observations.

T2015 searched for line signals in the 2–6 keV energy range using spectra extracted from a $10'$ radius circle. (see their figure 12 for the limit in EW). They used the Suzaku Crab Nebula observation to correct their effective area and estimated a systematic sensitivity to a weak line feature of less than 2 eV in EW from the maximum line flux in the Crab spectrum.

We note that in the XIS case the best-fit flux fluctuation amplitude is larger than the statistical error level over most energy bins. Therefore, the flux limit was determined by the systematic error estimated from the Crab spectra. Contrary to the XIS case, the SXS statistical errors are larger than the systematic one estimated from the SXS Crab observation at least above 6 keV (figure 5). The Crab systematic errors are smaller (< 1 eV) than those of the XIS.

In some energy ranges, the current SXS observation provides smaller EW limits than XIS. However, this does not always translate into a smaller limit in line flux (F_{Line}) or intensity (f_{Line}) as explained below. These values are related to the source flux intensity (f_{source}; the cluster and AGN flux over the relevant energy range in this case) and observed sky area (Ω) as follows.

$$F_{\mathrm{line}} = EW \times F_{\mathrm{source}}. \tag{5}$$

$$f_{\mathrm{line}} = F_{\mathrm{line}}/\Omega = EW \times F_{\mathrm{source}}/\Omega = EW \times f_{\mathrm{source}}. \tag{6}$$

Given the Perseus cluster surface brightness distribution (including the AGN flux) and $\Omega(SXS; 3' \times 3')/\Omega(XIS; r < 10') \sim 1/36$ (table 4), we estimate $f_{\mathrm{sou,SXS}}/f_{\mathrm{sou,XIS}} \sim 12$ and $F_{\mathrm{sou,SXS}}/F_{\mathrm{sou,XIS}} \sim 3$. Therefore as given in the last equation above for the same EW limit, the SXS f_{line} limit is larger than the XIS one by a factor of > 10. Even if the SXS EW limit is half of the XIS limit, the SXS flux limit is 6 (12/2) times larger than the XIS one.

As shown in figure 13 the difference between the two observations is consistent with the above estimation. For the XIS spectra below 6 keV, the effective area systematic error hinders the sensitivity to a weak line. Above this energy range the cluster Fe line emission, instrumental features, and continuum background along with the decreasing effective area reduce the sensitivity. In contrast, the SXS high resolution spectroscopy resolves and localizes these plasma and instrumental features, resulting in less contamination around these features. The decreasing SXS effective area dominates its sensitivity reduction.
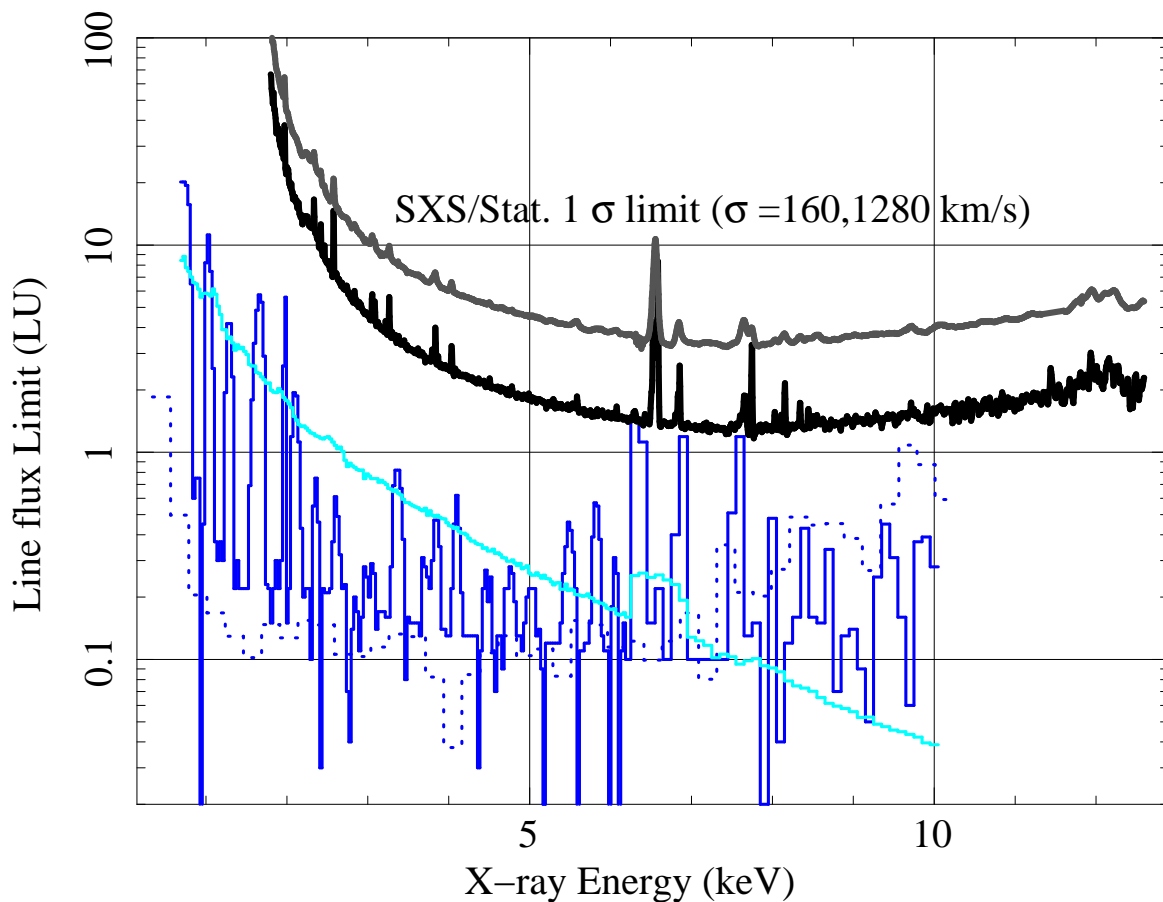

Fig. 13.

Limits (1σ) on the line surface brightness in unit of photons cm^{-2} s^{-1} sr^{-1} (LU). The current SXS result (1σ) with σ_{Line} = 160 km s^{-1} and 1280 km s^{-1} (black and grey colors respectively; scaled from values in figure 5 and calculated in subsection 3.1) are compared with the Suzaku XIS results (1σ) from T2015. The XIS limits refer to systematic (1 eV in EW; light blue), statistical (blue), and for the Ursa Minor dwarf galaxy (dotted line; Loewenstein et al. 2009; (3σ)), respectively.

Table 4. Hitomi SXS and Suzaku XIS and observations.

Detector	Area *	FOV †	exp♯	Area× exp	Area× exp × FOV	E band ‡	ΔE §
	(cm^2)	(arcmin^2)	(ks)	(10^6 cm$^2\cdot$ s)	10^9 cm$^2\cdot$ s $\cdot$ arcmin^2)	(keV)	(eV)
SXS	100	9	289	29	0.26	2-12	5
XIS/FI	260	320	1040	270	86.5	-	-
XIS/BI	260	320	530	138	44.1	-	-
total	520	-	-	408	130.6	2–6	80-150

∗ Effective area at energy of 3.5 keV.

† Detector's field of view.

♯ Exposure time.

‡ Energy band

§ Energy resolution in FWHM (full-width-half-maximum).

Constraints on the X-ray flux of dark matter decay lines have been derived using various targets and instruments with various band passes. For example, Sekiya et al. (2016) used a large quantity of X-ray diffuse background (XDB) data from Suzaku XIS in a search for the dark matter signal from our Galaxy in the 1–7 keV energy range. Perez et al. (2017) used NuSTAR observations of the Galactic center in the 3–80 keV range.

To compare the sensitivity to a dark matter signal among different observations , instead of the dark matter decay rate (Γ_{DM}) itself, we use the line flux density (f_{line}) divided by (Σ_{DM}), which is proportional to Γ_{DM}, as given in equation 2. For the Perseus cluster Σ_{DM} within the SXS field of view is calculated using the mass $(6-8) \times 10^{12}\ M_\odot$ used in Aharonian et al. (2017). Note that this and other Σ_{DM} estimations given below are uncertain up to a factor of two.

To estimate the line flux limit from SXS observations we adopt the statistical errors, which are larger than or comparable to the Crab systematic ones (figure 5). Table 5 shows the resulting limits along with previous analyses. Compared with the XIS limit in T2015 for the same target but covering a larger area, current SXS limits are larger (weaker) at energy below 7–8 keV and comparable at higher energies.

Because the cluster X-ray brightness is more strongly concentrated toward the center (roughly proportional to square of gas density) than the estimated dark matter decay flux (proportional to dark matter density), observations limited to the central parts such as the SXS one have higher plasma flux (background) and smaller signal-to-background ratio than more extended ones such as the XIS observations. This is a primary factor for the stronger limit on Γ_{DM} obtained by the XIS than the current SXS result at energies below 7–8 keV. Above this energy range, the XIS sensitivity is limited by instrumental background , while SXS one is limited only by the decreasing effective area and photon statistics, as described in sub-subsection 4.1.4.

For the energy range of 1–7 keV, the XDB observations (Sekiya et al. 2016) provides stronger limit on the line flux and Γ_{DM} than other limits (table 5). This is largely due to the much lower X-ray flux density in the XDB than those in X-ray bright galaxies and clusters as well as the larger solid angle and deeper observations. Above about 7 keV, this XIS observation suffers from the instrumental background in the same way as the XIS Perseus observation in T2015.

For energies above 7 keV, the NuSTAR observations of the Galactic center in Perez et al. (2017) provides a strong limit on the line flux and on Γ_{DM} . This is largely due to a large

solid angle of NuSTAR (effective solid angle of $> 10^4$ arcmin^2 and detector area of 4-11 cm^2 as given in their table 1). The large Σ_{DM} toward the Galactic center region also contributes to the strong limit.

Our flux limits along with the assumed Σ_{DM} are translated into those on the sterile neutrino mass-mixing angle plane as shown in figure 14.
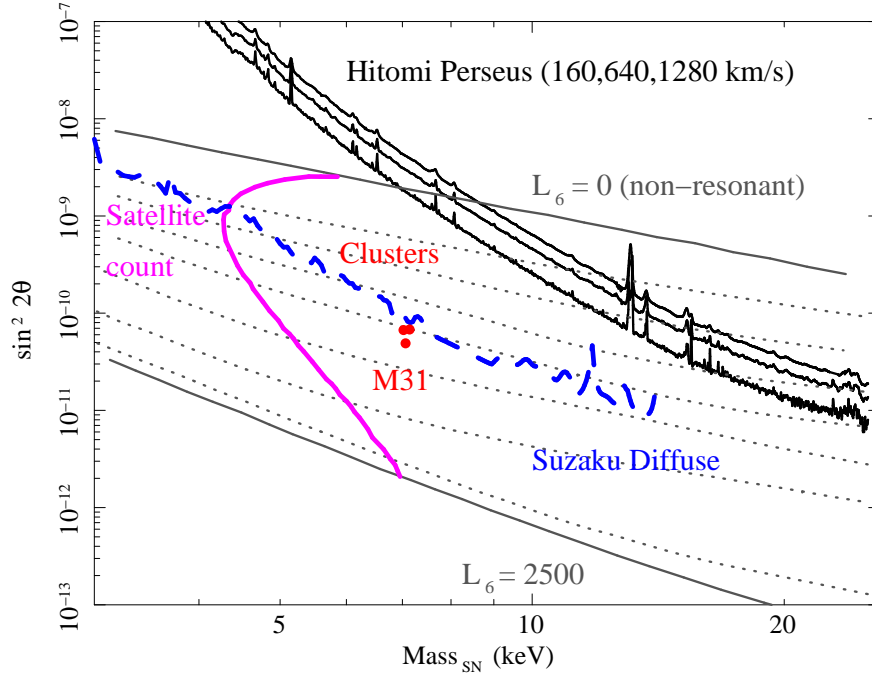

Fig. 14. Constraint from Hitomi observations of the Perseus cluster core are shown by the black solid line on the sterile neutrino mass-mixing angle plane. The 3σ line flux limit with velocity dispersions at 160, 640, and 1280 in $\mathrm{km\ s^{-1}}$ for lower to higher limits and the dark matter surface density, $\Sigma_{\mathrm{DM}} = 1750$ $M_\odot$ pc^{-2}, are used along with equations in T2015 and a dark matter decay rate from ?. The 3σ limits (correcting for the look elsewhere effect) from the Suzaku X-ray diffuse background spectra are shown by the blue dashed line (Sekiya et al. 2016). The red data points indicate the claimed signals from M31 (Boyarsky et al. 2014) and stacked galaxy clusters (Bulbul et al. 2014). Along the gray horizontal curves, the sterile neutrino relic abundance from the (non-)resonant production coincides with the observed dark matter mass density, for a given lepton asymmetry per entropy density, $L \times 10^6 = L_6 = 0, 4, 8, 12, 16, 25, 70, 700, 2500$, are shown. Here we utilize the public code `sterile-dm` (Venumadhav et al. 2016) to calculate the relic abundance. The region of parameter space left of the magenta curve is disfavored by the satellite number count (Cherry & Horiuchi 2017).

Our analysis confirms importance of the instrumental calibration to maximize its spectroscopic capability. Firstly, in our analysis, effective area calibration on a fine energy grid limits the systematic uncertainty of weak line fluxes. This is particularly crucial with bright X-ray sources like galaxy clusters and the Galactic center. Without the Hitomi observations of the Crab Nebula, a line free bright X-ray source, we could not examine the effective area uncertainty. Secondly, the energy scale and response should also be stable and calibrated well for separating source features from statistical noise and atomic or instrumental features without a-priori knowledge of position and Doppler velocity. In the Hitomi case, these were calibrated without the originally planned per-pixel, simultaneous X-ray energy calibration using the Modulated X-ray Source. For the new mission, this system will be used to improve spectroscopic performance. See e.g., Kilbourne et al. (2018) for the SXS calibration.

In addition to the instrumental features, atomic line emission parameters should also be calibrated and improved. The obtained lack of additional lines (subsection 3.3) supports the accuracy level of the current plasma modeling, as examined in H2018-A. As shown in H2018-A and this study (figures 7-12) a forest of weak atomic lines are expected to appear depending mainly on the source plasma temperature and metal abundances. Most weak features have not yet been observed and hence have uncertainties in their positions and emissivities. Uncertainties in the plasma emission modeling also limit the identification of new features. In fact the SXS Perseus spectra suggest the presence of charge exchange emission on top of the thermal emission (subsection 3.3). Once these atomic features are resolved and modeled accurately, the analysis should become more suitable for carrying out blind searches. Alternatively, these atomic contamination features may be avoided by observing X-ray faint sources that have lower dark matter densities but better dark matter to plasma emission background ratios.

Table 5. Limits on the dark matter signal.

Origin	Target	$\Sigma_{\rm DM}$ [*]	Ins. [†]	Energy	f limit [‡]	$f/\Sigma_{\rm DM}$	$\Gamma_{\rm DM}$ [‖]
				keV	(1σ; LU)		10^{-28} s^{-1}
This ($\sigma_{\rm Line} = 640$ km s^{-1})	Perseus	1750	SXS	2	30	170	80
–	–	–	–	5	3.0	15	20
–	–	–		8	2.0	12	20
T2015	Perseus (R$< 10'$)	800	XIS	2	2.0	25	10
–	–	–	–	5	0.3	4	4
–	–	–	–	8	0.5	6	10
Bulbul et al. (2014)	Perseus	820	XMM/MOS	3.5	1.9	23	18
Sekiya et al. (2016)	XDB	30	XIS	1–7	3×10^{-3}	1.0	1
Perez et al. (2017)	GC	300	NuSTAR	3-7	2×10^{-1}	7	7
–	–	–		7-100	2×10^{-2}	0.7	7

[*] Dark matter surface mass density in units of $M_\odot$ pc^{-2}.

[†] Mission and instrument name.

[‡] X-ray line flux 1σ limit. We assume a Gaussian distribution for the error range.

[§] Given in units of 10^{-4} LU pc$^2/M_\odot$.

[‖] Dark matter decay rate limits corresponding to the line flux limit as in equation 2.

Aharonian et al. (2017) used the SXS high energy resolution spectrum and did not confirm the 3.5 keV signal reported in Bulbul et al. (2014). We extended this search into the full observed energy band of 2–12 keV We have demonstrated the unique advantages of high resolution spectroscopy for weak line searches and provided a pilot study for future reference.

We provide lists of possible line emission as well as line absorption features (table 3). These signals may represent statistical fluctuations or, in some cases, the first hints of unmodeled atomic lines or lines of other origin. These should be examined with future laboratory and cosmic X-ray experiments. Hint of faint line features possibly originating from Zn and charge exchange emission demonstrates the vast potential of high resolution spectroscopy of cosmic plasma. These features will be resolved by deep and targeted observations and be unique probes for cosmic plasma.

We found no significant unidentified line emission nor absorption (section 3.3). The line flux upper limits as functions of energy and their dependence on intrinsic line width are displayed in figure 5 and table 5.

Due to the smaller grasp and shorter exposure of the current observation compared with those of previous searches, our flux limit is not largely stronger than those claimed previously. However, we should examine carefully the previous analyses based on lower energy resolution spectra. As discussed in section 1 some original claimed detected fluxes of a 3.5 keV line (Bulbul et al. 2014) are in conflict with other analyses, including those from high energy resolution spectra. This may indicate that some of these reports underestimated systematic uncertainties for weak lines. Accordingly, our results are complementary to past studies for X-ray line searches, utilizing a target with one of the highest dark matter column densities in the nearby universe.

The small grasp of the SXS is an impediment to measurement of fluxes of possible unidentified faint signals. Even ignoring background and other instrumental systematic errors, to detect and resolve the signal more robustly than previous claims, at least 10 line photons are required. This approximately corresponds to the 3σ photon-limit sensitivity as estimated in Kitayama et al. (2014) with the designed SXS capability. The expected sensitivities with 1 Ms exposure are about 0.3 (0.5 keV), 0.06 (1–5 keV), and 0.1 (10 keV), all in LU at energies given in parentheses, for a narrow line emission. These fluxes are not significantly lower than the level constrained previously (see table 5 for examples). Additionally lines can possess a variety of intrinsic widths and can be particularly broad in massive objects. Therefore, to detect such

34

faint unidentified signals, much deeper data or larger grasp with good energy resolution is required.

The next opportunity for astronomical high resolution non-dispersive X-ray spectroscopy will be the calorimeter on the JAXA-NASA Hitomi recovery mission, XRISM (**?**). This will have basic design and capabilities inherited from Hitomi , and will observe a variety of dark matter-rich systems. With XRISM , the energy range will be extended down to 0.5 keV and much longer observation times employed. Kitayama et al. (2014) discussed detailed strategies for the dark matter search using SXS-type spectroscopy. If any unidentified candidate signals are suggested by theories or by X-ray and other observations, the XRISM instrument will be the first to identify or reject those signals.

References

Abazajian, K., Fuller, G. M., & Tucker, W. H. 2001, ApJ, 562, 593

Abazajian, K. N. 2017, Phys. Rep., 711, 1

Adhikari, R., Agostini, M., Ky, N. A., et al. 2017, Journal of Cosmology Astroparticle Physics, 1, 025

Aharonian, F. A., Akamatsu, H., Akimoto, F., et al. 2017, ApJL, 837, L15

Arnaud, K. A. 1996, Astronomical Data Analysis Software and Systems V, 101, 17

Angelini, L., Terada, Y., Dutka, M., et al. 2018, Journal of Astronomical Telescopes, Instruments, and Systems, 4, 011207

Arcadi, G., Dutra, M., Ghosh, P., et al. 2018, European Physical Journal C, 78, #203

Bae, K. J., Kamada, A., Pei Liew, S., & Yanagi, K. 2018, Journal of Cosmology Astroparticle Physics, 1, 054

Baur, J., Palanque-Delabrouille, N., Yèche, C., et al. 2017, Journal of Cosmology Astroparticle Physics, 12, 013

Boyarsky, A., Ruchayskiy, O., Iakubovskyi, D., & Franse, J. 2014, Physical Review Letters, 113, 251301

Boyarsky, A., Franse, J., Iakubovskyi, D., & Ruchayskiy, O. 2015, Physical Review Letters, 115, 161301

Bulbul, E., Markevitch, M., Foster, A., et al. 2014, ApJ, 789, 13

Cherry, J. F., & Horiuchi, S. 2017, Phys. Rev. D, 95, 083015

Cappelluti, N., Bulbul, E., Foster, A., et al. 2018, ApJ, 854, 179

Cash, W. 1979, ApJ, 228, 939

Figueroa-Feliciano, E., Anderson, A. J., Castro, D., et al. 2015, ApJ, 814, 82

Gu, L., Kaastra, J., Raassen, A. J. J., et al. 2015, A&A, 584, L11

Hitomi Collaboration, Aharonian, F., Akamatsu, H., et al. 2016, Nature, 535, 117

Hitomi Collaboration, Aharonian, F., Akamatsu, H., et al. 2017, Nature, 551, 478

Hitomi Collaboration, Aharonian, F., Akamatsu, H., et al. 2018a, PASJ, 70, 14

Hitomi Collaboration, Aharonian, F., Akamatsu, H., et al. 2018b, PASJ, 70, 9

Hitomi Collaboration, Aharonian, F., Akamatsu, H., et al. 2018c, PASJ, 70, 11 (H2018-T)

Hitomi Collaboration, Aharonian, F., Akamatsu, H., et al. 2018d, PASJ, 70, 12 (H2018-A)

Hitomi Collaboration, Aharonian, F., Akamatsu, H., et al. 2018e, PASJ, 70, 13

Iizuka, R., Hayashi, T., Maeda, Y., et al. 2018, Journal of Astronomical Telescopes, Instruments, and Systems, 4, 011213

Kaastra, J. S., Mewe, R., & Nieuwenhuijzen, H. 1996, UV and X-ray Spectroscopy of Astrophysical

and Laboratory Plasmas, 411

Kaastra, J. S., Paerels, F. B. S., Durret, F., Schindler, S., & Richter, P. 2008, Space Sci. Rev., 134, 155

Kelley, R. L., et al. 2018, J. Astron. Telesc. Instrum. Syst., submitted

Kent, S. M., & Sargent, W. L. W. 1983, AJ, 88, 697

Kilbourne, C. A., Adams, J. S., Brekosky, R. P., et al. 2018, Journal of Astronomical Telescopes, Instruments, and Systems, 4, 011214

Kitayama, T., Bautz, M., Markevitch, M., et al. 2014, arXiv:1412.1176

Kilbourne, C. A., Sawada, M., Tsujimoto, M., et al. 2018, PASJ, 70, 18

Koyama, K., Kataoka, J., Nobukawa, M., et al. 2014, arXiv:1412.1170

Loewenstein, M., Kusenko, A., & Biermann, P. L. 2009, ApJ, 700, 426

Okajima, T., Soong, Y., Serlemitsos, P., et al. 2016, Proc. SPIE, 9905, 99050Z

Perez, K., Ng, K. C. Y., Beacom, J. F., et al. 2017, Phys. Rev. D, 95, 123002

Prokhorov, D., & Silk, J. 2010, ApJL, 725, L131

Maeda, Y., Sato, T., Hayashi, T., et al. 2018, PASJ, 70, 19

Neronov, A., Malyshev, D., & Eckert, D. 2016, Phys. Rev. D, 94, 123504

Rasmussen, A. P., Kahn, S. M., Paerels, F., et al. 2007, ApJ, 656, 129

Roszkowski, L., Sessolo, E. M., & Trojanowski, S. 2018, Reports on Progress in Physics, 81, 066201

Ruchayskiy, O., Boyarsky, A., Iakubovskyi, D., et al. 2016, MNRAS, 460, 1390

Sekiya, N., Yamasaki, N. Y., & Mitsuda, K. 2016, PASJ, 68, S31

Smith, R.K & Brickhouse, N.S. 2001, ApJ, 556, L91

Smith, R. K., Odaka, H., Audard, M., et al. 2014, arXiv:1412.1172

Takahashi, T., Kokubun, M., Mitsuda, K., et al. 2016, Proc. SPIE, 9905, 99050U

Takahashi, T., et al.2018, J. Astron. Telesc. Instrum. Syst., submitted

Tamura, T., Iizuka, R., Maeda, Y., Mitsuda, K., & Yamasaki, N. Y. 2015, PASJ, 67, 23 (T2015)

Venumadhav, T., Cyr-Racine, F.-Y., Abazajian, K. N., & Hirata, C. M. 2016, Phys. Rev. D, 94, 043515

Appendix 1 Associated tables and plots

Fig. 15. The Perseus core spectrum and detected line emission signals. The vertical axis is given by line detection significance in σ. The continuum emission is modeled by a single temperature CIE model and subtracted. Atomic line identifications are shown. Dashed and dotted horizontal lines show 5 and 3 σ detections.

Table 6. Possible identification and associated ines from the SPEX database.

(1) Nr	(2) ele	(3) stage	(4) Energy	(5) Emi	(6) Up
48	Si	XIV	2646.5	1.1e-03	10p
54	Si	XIV	2651.1	7.9e-04	11p
57	Si	XIV	2654.6	3.0e-04	12p
60	Si	XIV	2654.6	6.0e-04	12p
66	Si	XIV	2657.4	4.7e-04	13p
72	Si	XIV	2659.6	3.7e-04	14p
78	Si	XIV	2661.3	3.0e-04	15p
30	Ni	XXVIII	10556.4	7.9e-06	7p
33	Ni	XXVIII	10607.8	2.6e-06	8p
36	Ni	XXVIII	10607.8	5.1e-06	8p

(1) Nr: Identification number defined in the SPEX database.

(2) Ele: Element name.

(4) Energy: rest frame energy in eV.

(5) Emi: emissivity for a 4.3 keV plasma with a certain emission measure normalizaed by that of Fe XXV resonance (the strongest one).

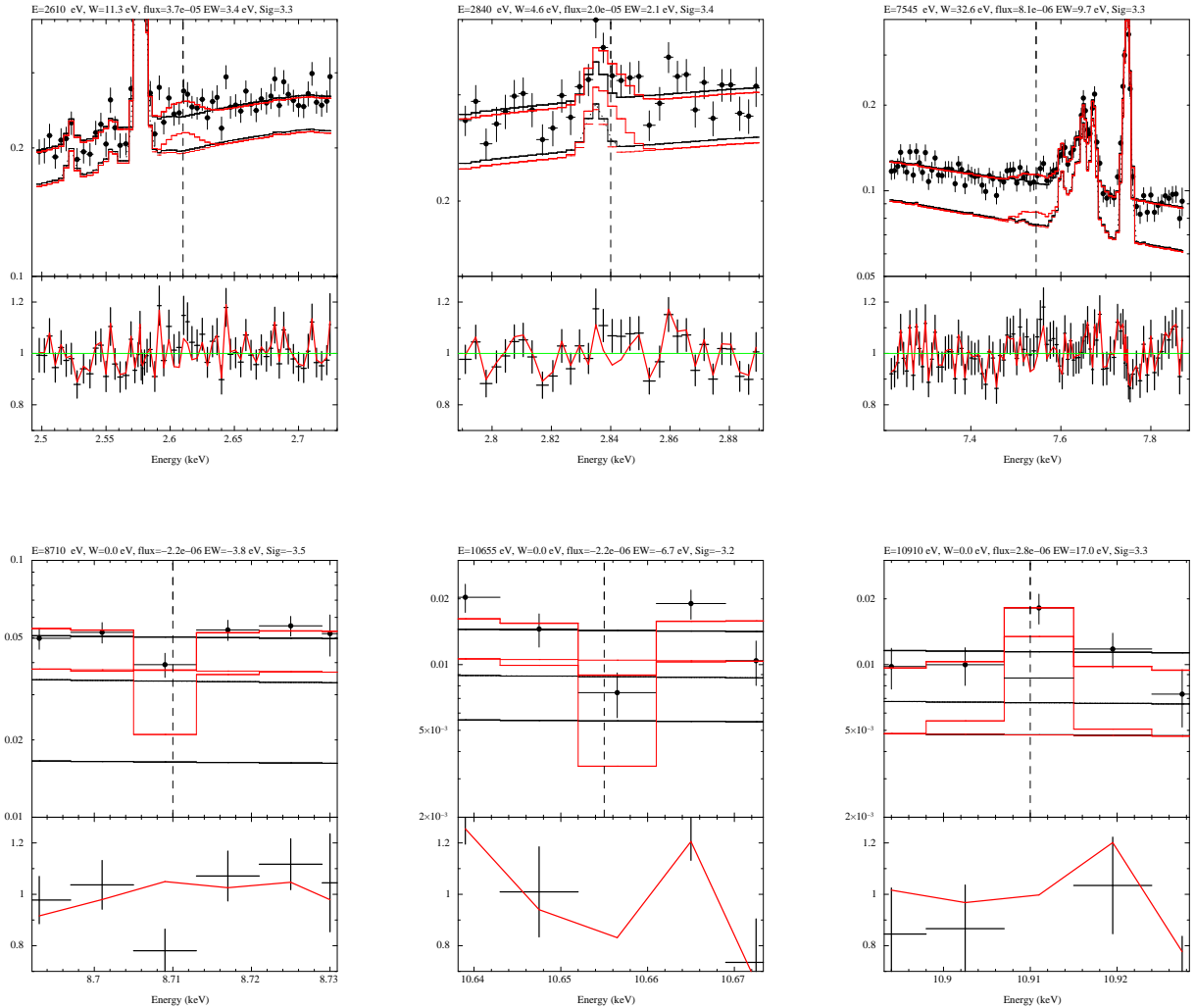(6) Up: Upper level electron configulation.

Fig. 16. Zooming-in spectral fitting results from the energy ranges where possible line emission features are found. Units of top and bottom panels are counts s^{-1} keV^{-1} and data to model ratio, respectively. Position and other best-fit parameters of the input Gaussian line are given in each panel. Black (red) histograms and residuals are for models without (with) the line feature at the position shown in the dashed vertical line. Note that spectrum is rebined coarsely for plotting purpose but for fitting we use the original 1 eV bin size.
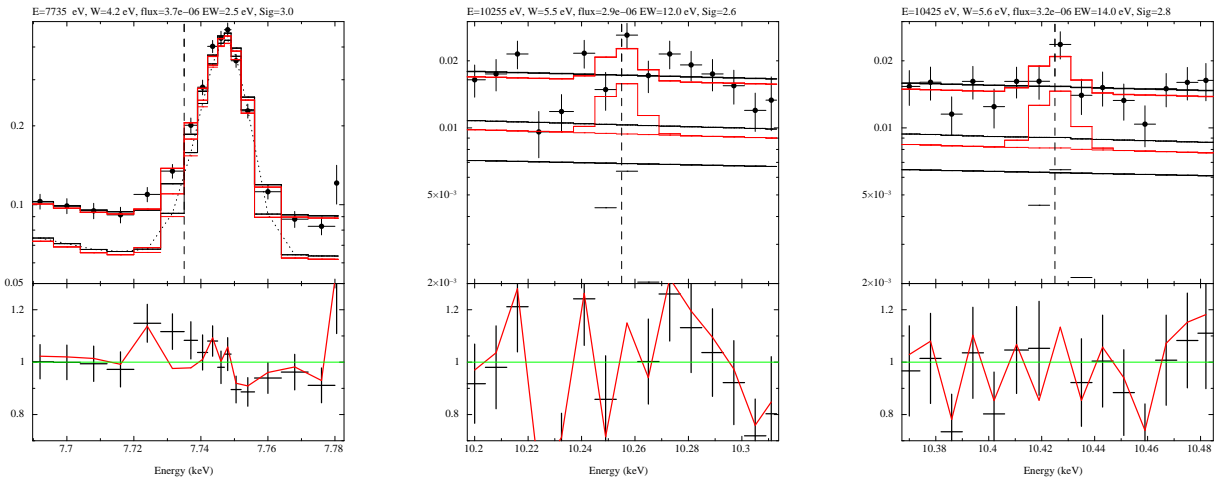
Fig. 17. Same plots as figure 16, but for $\sigma_{\mathrm{Line}} = 160~\mathrm{km~s}^{-1}$ and emission signals.
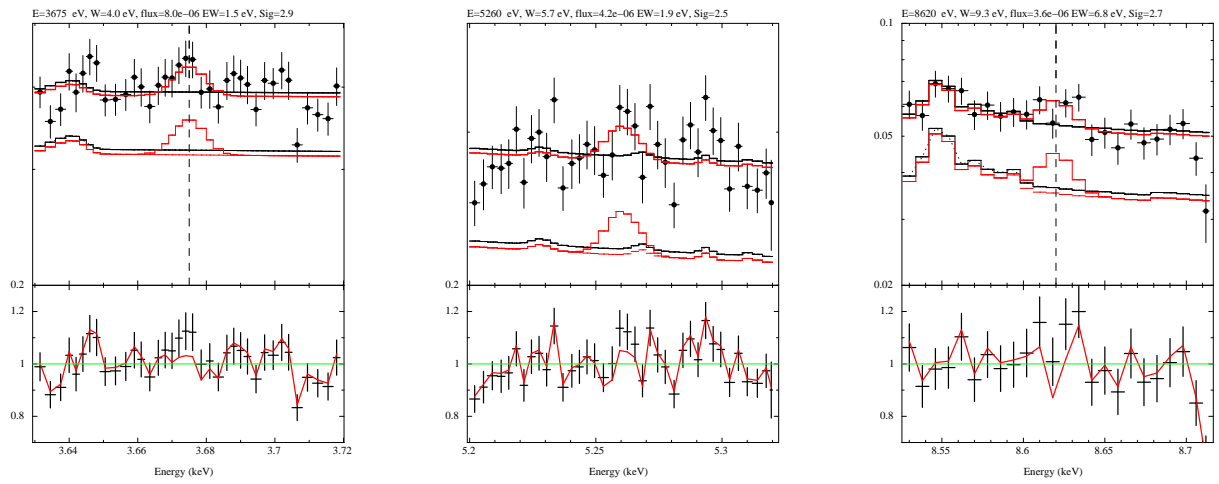

Fig. 18. Same plots as the previous one, but for $\sigma_{\mathrm{Line}} = 320~\mathrm{km~s}^{-1}$ and emission signals. See Table 3.
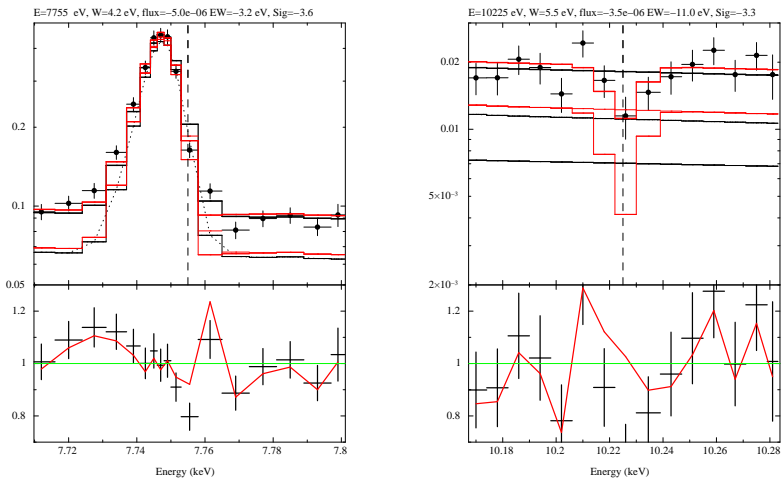
Fig. 19. Same plots as the previous one, but for $\sigma_{\mathrm{Line}} = 160\ \mathrm{km\ s^{-1}}$ and absorption signals.